Modelling Microscale Fuel Cells

by

Aimy Ming Jii Bazylak

B.E., University of Saskatchewan, 2003

A Thesis Submitted in Partial Fulfillment of the Requirements for the Degree of

MASTER OF APPLIED SCIENCE

in the Department of Mechanical Engineering

© Aimy Ming Jii Bazylak, 2005

University of Victoria

Supervisors: Dr. Ned Djilali & Dr. David Sinton, (Dept. of Mechanical Engineering)

Abstract

The focus of this work is to investigate transport phenomena in recently developed microscale fuel cell designs using computational fluid dynamics (CFD). Two microscale fuel cell systems are considered in this work: the membraneless microfluidic fuel cell and a planar array of integrated fuel cells.

A concise electrochemical model of the key reactions and appropriate boundary conditions are presented in conjunction with the development of a three-dimensional CFD model of a membraneless microfluidic fuel cell that accounts for the coupled flow, species transport and reaction kinetics. Numerical simulations show that the fuel cell is diffusion limited, and the system performances of several microchannel and electrode geometries are compared. A tapered-electrode design is proposed, which results in a fuel utilization of over 50 %.

A computational heat transfer analysis of an array of distributed fuel cells on the bottom wall of a horizontal enclosure is also presented. The fuel cells are modelled as flush-mounted sources with prescribed heat flux boundary conditions. The optimum heat transfer rates and the onset of thermal instability are found to be governed by the length and spacing of the sources and the width-to-height aspect ratio of the enclosure. The transition from a conduction-dominated to a convection-dominated regime occurs over a range of Rayleigh numbers. Smaller source lengths result in higher heat transfer rates due to dramatic changes in Rayleigh-Bénard cell structures following transition.

Table of Contents

Acknowledgments

List of Figures

List of Tables

Nomenclature

Chemical Formulas

CO	Carbon monoxide
CO_2	Carbon dioxide
$(COOH)_{ads}$	Adsorbed COOH
e^-	Electron
H^+	Proton
H_2O	Water
H_2SO_4	Sulfuric Acid
$HCOOH$	Formic acid
OH	Hydroxide
O_2	Oxygen
Pd	Palladium
Pt	Platinum
Pt^o	Free platinum site
Ru	Ruthenium

Variables

A	Pre-exponential factor
A_{area}	Cross-sectional area of microchannel
B	Mean amplitude of heat flux modulation
C_i	Concentration of point, i

C_i^{mixed}	Concentration of perfectly mixed solution at point, i
C_i^o	Concentration of solution at point i in the absence of mixing
C_p	Specific heat capacity
D_h	Hydraulic diameter
D_i	Diffusion coefficient
E	Potential at electrode
E^o	Standard potential at electrode
E_a	Activation energy
E_{rev}	Reversible potential
F	Faraday constant
G^o	Gibbs free energy
$\bar{g}$	Acceleration of gravity
H	Height of plenum
h	Channel height
h^*	Heat transfer coefficient
J_i	Flux of species, i
k	Rate constant
k^*	Thermal conductivity
L	Length of heat source
$\dot{m}$	Mass flow rate
N	Total number of cells
Nu	Nusselt number

Nu_{avg}	Temporally-averaged and spatially-averaged Nusselt number
n	Number of electrons
n_{rds}	Number of electrons in rate determining step
n_r	Index of refraction
P	Static pressure
P^*	Dimensionless pressure
Pr	Prandtl number
$\dot{q}$	Power
q_L''	Source heat flux
q_S''	Spacing heat flux
R	Gas constant
Ra	Rayleigh number
Re	Reynolds number
R_{cell}	Ionic resistance of electrolyte
R_i	Net rate of production of species i
S	Length of spacing between sources
T	Temperature
T_L	Top wall temperature
T_{max}	Maximum temperature of heat source surface
ΔT	Difference between local temperature and top wall temperature $(= T - T_L)$
t	Time
t^*	Dimensionless time

U	Average fluid velocity
V_{max}	Maximum velocity
$V_{max,avg}$	Temporally averaged maximum velocity
v	Rate law
$\vec{v}$	Velocity vector
$\vec{v}^{*}$	Dimensionless velocity vector
Δx	Diffusive mixing region width
Y_i	Local mass fraction of species, i
y	Distance fluid travels downstream

Greek

α	Charge transfer coefficient
α^{*}	Thermal diffusivity of air
α_{abs}	Hemispherical surface absorptivity
$\alpha_{abs,\lambda}$	Wavelength dependent surface absorptivity
β	Thermal expansion coefficient
δ	Oscillation amplitude
ε	Hemispherical surface emissivity
ε_{λ}	Wavelength dependent surface emissivity
ε_n	Normal surface emissivity
Λ^{o}	Limiting equivalent electrolyte conductance
λ_o	Wavelength of electromagnetic radiation
λ_{+}^{o}	Limiting conductance of cation

λ_-^o	Limiting conductance of anion
μ	Dynamic viscosity
η	Overpotential
ϕ	Phase shift
ρ	Fluid density
τ	Period of oscillation
θ_{ad}	Coverage by the underpotential deposition of hydrogen and anion species
θ_{CO}	Coverage of platinum sites by carbon monoxide
θ_{COOH}	Coverage of platinum sites by $(COOH)_{ads}$
υ	Kinematic viscosity
ν_+	Number of cation moles
ν_-	Number of anion moles
ω	Frequency of modulation
χ	Apparent reaction order

Chapter 1   Introduction

1.1   Background and Motivation

A fuel cell is an electrochemical device that converts chemical energy from the chemical reaction of a fuel and oxidant into electricity [Larmine, (2003)]. There are many types of fuel cells, and they are usually classified in terms of their electrolyte. Fuel cells can provide power over a broad range from mWatts to MWatts, and several architectures have been devised. One technology undergoing intense development is the proton exchange membrane fuel cell (PEMFC), the operation of which is schematically illustrated in Figure 1.1. The architecture of the membraneless and integrated fuel cell systems studied here differ significantly from the PEMFC shown in Figure 1.1. However, all of these fuel cell systems rely on the conversion of chemical energy to electricity through oxidation and reduction reactions.

The PEMFC uses gaseous hydrogen as fuel and oxygen from the ambient air as oxidant. As shown in Figure 1.1, the membrane is sandwiched between the catalyst layers, gas-diffusion electrodes, and bipolar plates for the anode and cathode. From the two bipolar plates (containing fuel-left and oxidant-right flow channels), the reactants diffuse through the gas-diffusion electrodes and react at the catalyst layers. The protons released at the anode reaction travel through the ion conducting membrane, and the electrons released take an external path. The redox reactions at the anode and cathode drive the operation of the fuel cell by producing an electric potential and a current through an applied load.

Since all reactions taking place in fuel cells are surface based, the increase in the surface-to-volume ratio accompanying miniaturization leads to a fundamental

improvement in power density [McLean et al., (2000); Hahn et al., (2004)]. There are, however, mechanical limits to the miniaturization of conventional fuel cells [Lee et al., (2002)]: Machining graphite bipolar plates becomes difficult, and decreasing the size of the membrane and substrate decreases their supporting strength. In addition, the performance of miniaturized conventional fuel cells is limited by the ohmic polarization introduced by the membrane and related water management issues. Novel architectures are crucial for the success of microscale fuel cells [McLean et al., (2000)].

Micro-sized power sources are needed for small, portable devices capable of operating for long periods of time without recharging, such as cell phones and laptop computers through to more specialized devices such as remote sensors, global positioning devices, and *in vivo* diagnostic medical devices. It is predicted [Dyer, (2002)] that battery technology will not keep pace with these growing portable-power demands, particularly with the next wave of wireless technology, broadband mobile computing. Microstructured fuel cells have the potential to bridge the gap between battery technology and growing portable power demands, by facilitating longer run-times per weight and volume, quasi-instant recharge, and constant discharge. Recent developments in the field have benefited from micromanufacturing technology and biological and chemical lab-on-a-chip concepts that have been a driving force behind the recent developments of many microfluidic devices [Stone et al., (2004)].

1.2   Thesis Objectives

The objective of this work is to model microscale fuel cells using computational fluid dynamics (CFD). The thesis consists of two main parts: an investigation of the species transport and fuel utilization of recently introduced membraneless microfluidic fuel cells, and an investigation of heat transfer enhancement for planar microscale fuel cells through Rayleigh-Bénard natural convective flow and heat flux modulation.

The first part of the thesis is a computational analysis of a membraneless microfluidic fuel cell that uses the laminar nature of microflows to maintain the separation of fuel and oxidant streams. The fuel cell consists of a T-shaped microfluidic channel with liquid fuel and oxidant entering at separate inlets and flowing in parallel without turbulent or convective mixing. Recent experimental studies have established the proof-of-concept of such fuel cells and have also shown that their performance is greatly limited by poor fuel utilization. Improving fuel utilization while minimizing fuel-oxidant mixing in microfluidic fuel cells is the focus of this study.

The second part of the thesis is a computational analysis of the heat transfer due to an array of distributed fuel cells on the bottom wall of a horizontal enclosure. This work is motivated by the need for passive cooling through natural convection in the area of planar microscale fuel cells [Lee et al., (2002); Choban et al., (2002); Ferrigno et al., (2002); O'Hayre et al., (2003); Choban et al., (2004); Hahn et al., (2004); Cohen et al., (2005)]. In fuel cells and in microelectronics, increasing dissipative heat flux and increasing component density drive the need for more

efficient heat removal. The low thermal conductivity of commonly used organic materials intensifies the impact of this high heat flux by causing large temperature gradients between components and their substrate [Arik, (2004)]. Finned, air cooled heat sinks and liquid cooling are alternative designs for heat removal, but the major drawbacks of these designs are the associated increases in weight, cost and volume [Arik, (2004)]. In this study, the parameters governing Rayleigh-Bénard natural convective flows are investigated as a method of passive heat removal. In addition to steady state simulations, time dependent simulations are also performed to investigate the effects of modulating the heat flux boundary conditions of fuel cells. This work is motivated by the unsteady heat generation commonly produced by electronic components, and the potential for planar fuel cell systems to be designed and operated to take advantage of this heat flux modulation to enhance passive cooling through natural convective heat transfer.

The work in this thesis resulted in contributions to the literature [Bazylak et al., (2005a); Bazylak et al., (2005b)] and conference proceedings [Bazylak et al., (2004); Bazylak et al., (2005c)]. The specific contributions of this thesis are summarized in the following list:

Membraneless Microfluidic Fuel Cell

- A concise electrochemical model of the key reactions and appropriate boundary conditions is presented.

- A high aspect ratio rectangular geometry results in a two-fold increase in fuel utilization compared to a square geometry with the same hydraulic diameter.

- Fuel utilization increases non-linearly from 8 % to 23 % by decreasing the inlet velocity from 0.1 m s^{-1} to 0.02 m s^{-1}.

- A tapered-electrode microfluidic fuel cell design is proposed, which demonstrates a fuel utilization of over 50 %.

Distributed Heat Sources In An Enclosure

- A fuel cell spacing length equal to the fuel cell (heat source) length provides effective convective heat transfer, and increasing the fuel cell spacing further does not result in significant improvements.

- The transition from a conduction-dominated regime to a convection-dominated regime is found to be characterized by a range of Rayleigh numbers.

- At the transition region for very small sources, the Rayleigh-Bénard cell structure significantly grows to form fewer and larger cells, which accounts for higher heat transfer rates compared to configurations with larger fuel cells where the cell structure remains the same throughout the transition.

- In the convection-dominated regime, bifurcations in the Rayleigh-Bénard cell structures as well as further regime changes are observed, reflecting the flow patterns in the physical system.

- Including thermal radiation in the heat transfer model results in an increase in average Nusselt number for the source and a delay in thermal instability for the system.

- Modulating the heat flux boundary conditions of the heat sources sinusoidally with respect to time and introducing a phase shift between adjacent heat sources results in a decrease in average Nusselt number as well as a decrease in average temperature difference and maximum velocity in the system.
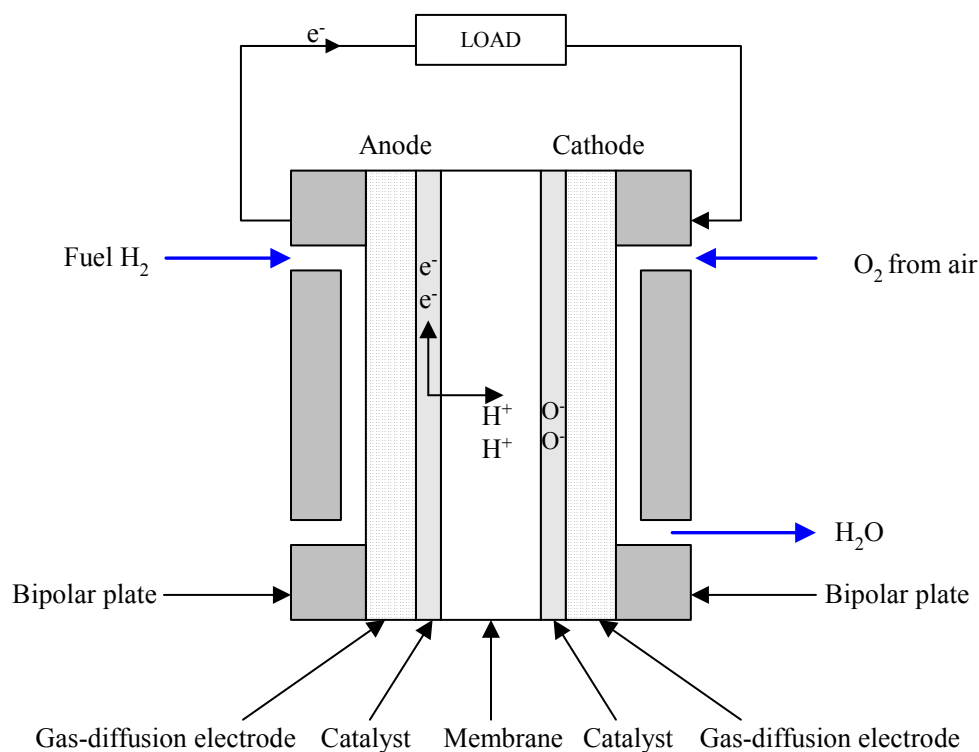
Figure 1.1. Schematic of a proton exchange membrane fuel cell. From the two bipolar plates (containing fuel-left and oxidant-right flow channels), the reactants diffuse through the gas-diffusion electrodes and react at the catalyst layers. Protons released at the anode reaction travel through the ion conducting membrane, and electrons released take an external path. The redox reactions at the anode and cathode drive the operation of the fuel cell by producing an electric potential and a current through an applied load.

Chapter 2   Membraneless Microfluidic Fuel Cell

2.1   Overview

In this chapter, a numerical analysis of a membraneless microfluidic fuel cell is presented. The three-dimensional model presented accounts for the coupled flow, species transport and electrochemical reactions at the electrodes. The results show that the microchannel and electrode geometries play significant roles in the fuel utilization of the fuel cell. A microchannel geometry and electrode placement design is proposed to improve the fuel utilization of this recently developed microscale fuel cell.

2.2   Background

Recently introduced membraneless microfluidic fuel cells [Choban et al., (2002); Choban et al., (2004); Ferrigno et al., (2002)] take advantage of the laminar nature of microflows to maintain the separation of fuel and oxidizer streams without the use of a membrane. A schematic of a microfluidic fuel cell and its operation are given in Figure 2.1. The geometry is that of a T-intersection, or T-mixer, which is commonly used in analytical microfluidic chips. The cross-stream mixing rate in such T-intersections is diffusion limited, and many studies have focused on increasing the mixing rate in such geometries [Stone et al., (2004)]. The microfluidic fuel cell, on the other hand, exploits the nature of this flow to achieve the separation of fuel and oxidant streams. The separation of fuel and oxidant is required to restrict reactions of oxidation and reduction to the appropriate electrode. Fuel is introduced at one inlet, and oxidant is introduced at the second inlet. Electrodes are placed along the walls to

complete the fuel cell, and oxidation at the anode and reduction at the cathode, together provide the cell potential. The fluid facilitates protonic conduction from one electrode to the other, and the electrons generated at the anode take an external path through an applied load. The length of the reaction channel is limited by the mixing of the two streams. The operation of the fuel cell will begin to fail when the two streams become mixed to the point that oxidation and reduction are no longer restricted to the appropriate electrodes.

Choban et al. (2002) were the first to demonstrate a membraneless fuel cell using formic acid and oxygen as reactants. They demonstrated that when two streams are flowing in parallel in the laminar regime, the streams remain separated, eliminating the need for a membrane. Ferrigno et al. (2002) demonstrated a millimeter-scale fuel cell using Vanadium as reactants. The advantage of this design is that it used the same species (Vanadium) as fuel and oxidant, which can be regenerated from a mixture of the products [Ferrigno et al., (2002)]. Choban et al. (2004) reported a Y-shaped microfluidic membraneless fuel cell system using formic acid and oxygen as reactants, which reached a current density of 0.4 mA cm^{-2}. The advantage of this system is that it uses acidic solutions to minimize the protonic resistance in the fluid. Both systems [Choban et al., (2004); Ferrigno et al., (2002)] were reported to be diffusion limited. In this work, a microchannel geometry with a high aspect ratio in the cross-stream direction, similar to that of Ferrigno et al. (2002), is investigated, as well as a square geometry similar to that of Choban et al. (2004). Microfluidic fuel cells have several advantages over conventional fuel cells: eliminating the membrane removes related ohmic losses, water management and

sealing issues; and since the fuel and oxidant streams flow together in the same channel network, the fuel cell size is reduced, the design is simplified, and the manifolding requirements are also reduced. In addition, research in this area can capitalize on recent advances in numerical [Orszag and Staroselsky, (2000)], experimental microfluidics [Sinton, (2004)], and microfabrication techniques [McDonald et al., (2000)]. Microfluidic fuel cells have the further advantage of using liquid fuels, which have high energy densities compared to gaseous fuels [Dyer, (2002)], particularly important in the context of portable power applications. However, current designs show relatively poor fuel utilization, on the order of 1 % [Choban et al., (2004)] to 10 % [Ferrigno et al., (2002)]. Modelling can provide insight into the parameters and geometry required to improve the performance of this technology.

2.3   Objectives

In this work a numerical analysis of a membraneless microfluidic fuel cell is presented. This work is one of the first CFD analyses of this technology. The model accounts for three-dimensional convective transport in conjunction with anodic and cathodic reaction kinetics. Appropriate boundary conditions for the CFD modelling of this system are developed here and implemented into the numerical model. A numerical investigation of the coupled flow, species transport and electrochemical aspects in this system is conducted. The results provide insight into the running parameters and both microchannel and electrode geometries required to achieve significantly improved performance. Finally, using the numerical simulation to guide

the electrode design process, an extended tapered-electrode design is proposed, and its performance is investigated.

2.4   Hydrodynamic and Mass Transport Model

A three-dimensional CFD model is applied to simulate the coupled flow, species transport, and chemical aspects of the microfluidic fuel cell. Due to the moderate liquid velocities, the internal heating due to viscous dissipation is ignored, and an isothermal system is assumed [Sharp et al., (2002)]. Refer to Appendix A for further details on why internal ohmic heating is neglected. Any heat transfer associated with the electrode reactions is also ignored. The following equations are solved for laminar flow in an inertial reference frame at steady state for incompressible and isothermal fluid flow. Neglecting body forces, the continuity and Navier Stokes equations for incompressible and isothermal flow are given by [Bird et al., (1960)]:

$$\nabla \cdot \vec{v} = 0 \tag{2.1}$$

$$\frac{\partial \vec{v}}{\partial t} + \nabla \cdot (\vec{v}\vec{v}) = -\frac{1}{\rho}\nabla P + \nabla \cdot (\upsilon \nabla \vec{v}) \tag{2.2}$$

where, P is the static pressure, ρ is the fluid density, $\vec{v}$ is the velocity vector, and υ is the kinematic viscosity. Low Reynolds numbers usually characterize liquid flows in microfluidic devices. After non-dimensionalizing the spatial coordinates, the velocity

field, time and pressure, the Reynolds number emerges as a key parameter in the Navier Stokes equation [Nguyen and Wereley, (2002)]:

$$Re\left(\frac{\partial \vec{v}^*}{\partial t^*} + \nabla \cdot \left(\vec{v}^* \vec{v}^*\right)\right) = -\nabla P^* + \nabla^2 \vec{v}^* \qquad (2.3)$$

where, $\vec{v}^*$ is the dimensionless velocity vector, t^* is the dimensionless time, and P^* is dimensionless pressure. For very small Reynolds numbers, $Re \ll 1$, the entire left side of equation (2.3) becomes negligible, which is generally an acceptable approximation for up to $Re \sim 1$ [Nguyen and Wereley, (2002)]. Reynolds numbers on the order of 10 characterize the liquid flow modelled in this work, therefore all terms of the Navier Stokes equation were included in the simulations. The conservation of species equation is given by:

$$\nabla \cdot \left(\rho \vec{v} Y_i\right) = -\nabla \cdot \vec{J}_i + R_i \qquad (2.4)$$

where, Y_i is the local mass fraction of species i, and R_i is the net rate of production of species i by chemical reaction. For the dilute approximation that is used in this model, the diffusion flux of species i is given by Fick's Law:

$$\vec{J}_i = -\rho D_i \nabla Y_i \qquad (2.5)$$

where, D_i is the diffusion coefficient for species i into the mixture. Losses due to protonic resistivity in the electrolytic solution were neglected since the protonic conductivity is significantly higher than that of Nafion 117, a commonly used membrane in conventional fuel cells. Further information regarding the conductivity of the electrolyte solution can be found in Appendix B.

2.5   Reaction Model

2.5.1   Formic Acid Oxidation

Formic acid (*HCOOH*) is an attractive fuel for fuel cells, as it has been reported to be electrochemically more active than methanol [Weber et al., (1996)]. The oxidation of formic acid is a well-studied, yet complex chemical reaction. The challenge is to provide a reasonable model for this highly non-linear, dual-pathway mechanism [Sun and Yang, (1999); Jiang and Kucernak, (2002)]. A platinum (*Pt*) catalyst is modelled due to its well-studied nature in regards to formic acid oxidation as well as use in conventional fuel cells.

The oxidation of formic acid on *Pt* occurs via a dual pathway mechanism [Rice et al., (2002)]. Through the first pathway, the dehydrogenation reaction, carbon dioxide (*CO₂*) is formed directly according to the generally accepted mechanism proposed by Capon and Parsons (1973):

$$Pt^o + HCOOH \rightarrow (COOH)_{ads} + H^+ + e^- \tag{2.6}$$

$$(COOH)_{ads} \rightarrow CO_2 + H^+ + e^- + Pt^o \tag{2.7}$$
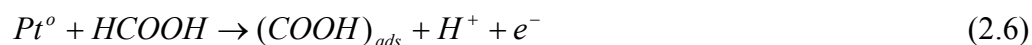
Through the second, the dehydration reaction, carbon monoxide (*CO*) is formed as a reaction intermediate.

$$HCOOH + Pt^o \rightarrow Pt - CO + H_2O \tag{2.8}$$

$$Pt^o + H_2O \rightarrow Pt - OH + H^+ + e^- \tag{2.9}$$

$$Pt - CO + Pt - OH \rightarrow 2Pt^o + CO_2 + H^+ + e^- \tag{2.10}$$

$$\text{Overall:} \, HCOOH \rightarrow CO_2 + 2H^+ + 2e^- \tag{2.11}$$
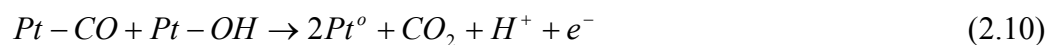
In the dehydration reaction, formic acid adsorbs onto the *Pt* surface, and an adsorbed *CO* intermediate is produced. Necessarily adsorbed hydroxyl (*OH*) groups are produced from the adsorption of water onto the *Pt* surface. These *OH* groups facilitate the required oxidation of the *CO* intermediate into gaseous CO_2. Since *OH* groups are not readily adsorbed onto *Pt* [Rice et al., (2002)], the *CO* reaction intermediate in the dehydration reaction may not become oxidized. The unfinished dehydration reaction results in adsorbed *CO*, which is a poison with respect to the *Pt* surface. In the case of poisoning, the *CO* intermediates remain strongly adsorbed and block the surface's active sites for further catalysis [Casado-Rivera et al., (2004)]. *CO* poisoning is fatal to the operation of the fuel cell; therefore the dehydrogenation reaction is preferred over the dehydration reaction.

With the proper catalyst, the oxidation of formic acid favors the direct pathway, the dehydrogenation reaction [Rice et al., (2002); Fonseca et al., (1983); Pletcher and Solis, (1982); Waszczuk et al., (2002)], through which CO_2 is formed directly. In a recent study, Rice et al. (2002) developed and used a proprietary catalyst

to selectively enhance the dehydrogenation pathway. The addition of surface additives to *Pt* for the purpose of increasing the oxidation rate of formic acid is widely researched. A *Pt* modified by palladium (*Pd*) catalyst has been found to be more active with respect to formic acid oxidation than a clean *Pt* surface, and this *Pt/Pd* catalyst has been also shown to be more active than a *Pt/Pd/Ru* or a *Pt/Ru* catalyst [Rice et al., (2002)]. An investigation by Jiang et al. (2002) also shows that the material structure and the electrode potential both affect the pathway in which formic acid is oxidized. At potentials above 0.376 V, the nanostructured *Pt* catalyst provides increasing tolerance to *CO* poisoning and thus the enhanced oxidation of formic acid through the direct pathway (dehydrogenation). Jiang et al. (2002) report that at potentials above 0.376 V, the poisoning rate remains quite low (0.3 % min^{-1}). In light of the catalyst research that has facilitated the dominance of the direct dehydrogenation reaction pathway, only the dehydrogenation pathway is modelled in this microfluidic fuel cell. Thus it will be assumed that the fuel cell is operating at a potential where poisoning is negligible and does not affect the operation of the fuel cell. Poisoning would not have a significant impact on the fuel utilization of the microfluidic fuel cell because the fuel cell was found to be diffusion limited. For example, if 5 % of Pt^o were unavailable due to poisoning at steady state, then the overall reaction rate would decrease by only 5 %.

The rate determining step occurs between *HCOOH* and the *Pt* electrode with the transfer of one electron, as shown in Equation (2.6) [Jiang and Kucernak, (2002); Fonseca et al., (1983)]. Modelling the oxidation of formic acid entails the formulation

of the rate constant and rate law governing the reaction. The rate constant in a chemical reaction is given by the Arrhenius equation:

$$k = Ae^{-E_a/RT} \qquad (2.12)$$

where, A is the pre-exponential factor, E_a is the activation energy, R is the gas constant and T is the temperature. The chemical reaction is also governed by the rate law, which is unique to each chemical reaction [Espenson, (1995)]. The rate law can also be affected by the coverage of Pt sites by CO and by $(COOH)_{ads}$ from the second step of the direct pathway, Equation (2.7). To account for this loss of kinetics, the rate law is given by:

$$v = k[HCOOH]^{\chi} \exp\left(\frac{\alpha \, n_{rds} F \eta}{RT}\right)(1 - \theta_{COOH} - \theta_{CO}) \qquad (2.13)$$

where, θ_{COOH} is the coverage of Pt sites by $(COOH)_{ads}$, and θ_{CO} is the coverage of Pt sites by CO, both in terms of a ratio between 0 and 1.

However, since the second step in the dehydrogenation reaction is believed to be faster than the rate determining step [Jiang and Kucernak, (2002)], it is assumed that the coverage of Pt sites by $(COOH)_{ads}$ is negligible ($\theta_{COOH} \approx 0$). It is also assumed that the fuel cell will be operating at a potential where poisoning is not an issue, so that coverage by CO is negligible ($\theta_{CO} \approx 0$). Therefore, the rate law is given by [Jiang and Kucernak, (2002)]:

$$v = k[HCOOH]^{\chi} \exp\left(\frac{\alpha\, nF\eta}{RT}\right) \qquad (2.14)$$

where, $[HCOOH]$ is the concentration of $HCOOH$ in the solution, χ is the apparent reaction order, α is the charge transfer coefficient, n_{rds} is the number of electrons released at the rate determining step, F is the Faraday constant, and η is the overpotential. In the rate determining step, one electron is released, therefore $n_{rds} = 1$ in Equation (2.14). The overpotential, η, is defined as:

$$\eta = E - E_{rev} \qquad (2.15)$$

where, E is the potential at the electrode, and E_{rev} is the reversible potential. In order to determine the reversible potential, the change in Gibbs free energy of formation is calculated for the formic acid oxidation reaction written as a reduction.

$$CO_{2(aq)} + 2H^{+}{}_{(aq)} + 2e^{-} \rightarrow HCOOH_{(aq)} \qquad (2.16)$$
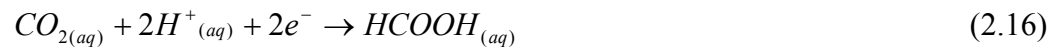
$$\Delta_f G^O = \Delta_f G^O_{\text{Pr}oducts} - \Delta_f G^O_{\text{Re}ac\tan ts} \qquad (2.17)$$

where, $\Delta_f G^O_{CO_{2(aq)}} =$ -385.98 kJ mol^{-1}, $\Delta_f G^O_{H+_{(aq)}} =$ 0 kJ mol^{-1} and $\Delta_f G^O_{HCOOH_{(aq)}} =$ -372.3 kJ mol^{-1} at 1 mol kg^{-1} standard state. Using Equation (2.16), the change in Gibbs free energy of formation is $\Delta_f G^O =$ 13.68 kJ mol^{-1}.

The standard potential is given by:

$$E° = \frac{-\Delta_f G^O}{nF}$$
(2.18)

where, $n = 2$, which is the number of electrons generated. The standard potential of formic acid oxidation is $E° = -0.07$ V (Standard hydrogen electrode), and the reversible potential is $E_{rev} = -0.18$ V. For $E = 0.6$ V reported by Fonseca et al. (1983), the overpotential is given by $\eta = 0.78$ V. According to the law of mass action [Metcalfe et al., (1970)], the rate determining step is a first order reaction, making $\chi = 1$. According to Capon and Parsons (1973), the charge transfer coefficient for the oxidation of formic acid on Pt is $\alpha = 0.51$. Similarly, Jiang and Kucernak (2002) reported the experimentally determined Tafel slope to be 132 mV dec^{-1} at 60 °C, which resulted in a charge transfer coefficient of $\alpha = 0.497$. The charge transfer coefficient assumed for our model, $\alpha = 0.497$, is in keeping with these works [Jiang and Kucernak, (2002); Capon and Parsons, (1973)].

For the rate determining step of the formic acid oxidation reaction, Fonseca et al. (1983) reported a rate constant of $k \cong 10^{-2}$ cm s^{-1} on a Pt catalyst modified with lead adatoms (atoms adsorbed on the electrode surface) at an electrode potential of 0.6 V (Standard hydrogen electrode) at 18 ± 2 °C. Pletcher and Solis (1982) reported a rate constant for the rate determining step of $k = 1.0 \pm 0.5 \times 10^{-2}$ cm s^{-1} at a potential of 0.6 V at room temperature for the oxidation of formic acid on a Pt anode with lead adatoms. Pletcher and Solis (1982) and Fonseca et al. (1983) both used the same coverage of 50 % of lead adatoms on their Pt surfaces, and obtained rate constants

within the same order of magnitude. The rate constant assumed for our model, $k = 1 \times 10^{-2}$ cm s^{-1}, is in keeping with these works [Fonseca et al., (1983); Pletcher and Solis, (1982)].

2.5.2   Oxygen Reduction

The protons released from the oxidation reaction at the anode diffuse through the solution in the cross-stream direction towards the cathode. At the cathode, the oxygen (O_2) from the oxidant stream, the protons and the electrons that travel through the external circuit combine to produce water in the oxygen reduction reaction:

$$\frac{1}{2}O_2 + 2H^+ + 2e^- \rightarrow H_2O \tag{2.19}$$

According to Markovic and Ross (1999), the rate of oxygen reduction on *Pt* can be expressed by the following current density:

$$i = nFk[O_2](1 - \theta_{ad})\exp\left(\frac{-\alpha F\eta}{RT}\right) \tag{2.20}$$

where, $[O_2]$ is the concentration of O_2 in the solution, and θ_{ad} is the coverage by the underpotential deposition of hydrogen and anion species. With an H_2SO_4 solution at potentials above 0.3 V, (bi)sulfate anions are the predominant adsorbed species.

For the oxidation reduction reaction on *Pt* in aqueous solutions of 0.5 M H_2SO_4 at 298 K and at 0.8 V, the reaction order is first order, and the rate constant, *k*,

varies according to the *Pt* crystal orientation as follows [Markovic and Ross, (1999)]:

k = 10 cm s^{-1}, 200 cm s^{-1} and 250 cm s^{-1} for *Pt*(111), *Pt*(100) and *Pt*(110), respectively. The activity on the *Pt*(111) surface is comparatively low because there is a strong adsorption of tetrahedrally bonded (bi)sulfate anions from sulfuric acid on this surface [Markovic and Ross, (1999)]. The differences between the activities for the various surfaces may be due to the surface's sensitivity to (bi)sulfate adsorption and the possible structure sensitivity to *O-O* bond breaking or *O-H* bond formation [Markovic and Ross, (1999)]. The *Pt*(110) surface is the most active surface for oxygen reduction. For our model, structural sensitivity of the *Pt* surface will be neglected.

Neglecting the structural sensitivity of the *Pt* surface, a rate constant of k = 250 cm s^{-1} is assumed for our model [Markovic and Ross, (1999)]. Based on this assumption, poisoning of the *Pt* surface is neglected, and the rate law can be written as:

$$v = k[O_2]\exp\left(\frac{-\alpha\, F\eta}{RT}\right) \qquad\qquad (2.21)$$

The standard potential for oxygen reduction is 1.46 V assuming $O_{2(aq)}$ is at its standard state of 1 mol/kg. The reversible potential for oxygen reduction is E_{rev} = 1.23 V, and from the definition of overpotential, η = -0.43 V at an electrode potential of 0.8 V. At this electrode potential, the charge transfer coefficient is α = 0.5 [Markovic and Ross, (1999)].

Both the formic acid oxidation and oxygen reduction reactions were assumed to be first order reactions. Several assumptions have been made in order to present a reasonable model for the implementation of redox reactions into the computational model. Surface poisoning has been neglected, the dominance of rate determining steps has been assumed, and electrochemical parameters have been approximated based on empirical results.

2.6   Membraneless Microfluidic Fuel Cell

The model was implemented in Fluent, a commercial finite-volume based CFD package. Dual processors were used to calculate the solutions generated from a hexagonal mesh, with typical run times of two hours. In all simulations, a hydraulic diameter of 100 μm was used for the inlet and outlet channels. Simulations involving the hydrodynamic and mass transport model are presented, followed by simulations including the reaction model.

The fuel and oxidant cross-stream diffusive mixing was quantified with the hydrodynamic and mass transport model. The operation of the fuel cell will begin to fail when the two streams become mixed to the point that oxidation and reduction are no longer restricted to the appropriate electrodes. The extent to which the fuel and oxidant become diffusively mixed is proportional to the diffusivity of the fuel in the solvent. The diffusivity also affects the mass transport of the fuel to the electrodes. The binary mixture is assumed dilute, and the diffusion coefficient is constant throughout. A diffusion coefficient of $D = 5\text{x}10^{-10}$ m^2 s^{-1} is assumed, which is a

typical value for the diffusion of relatively small molecules in an aqueous solution [Stone et al., (2004); Espenson, (1995)].

Pressure was applied to drive the flow, and a no-slip velocity condition was applied to the walls. These boundary conditions result in the formation of boundary layers with steep cross-stream velocity gradients, apparent in the velocity profiles plotted in Figure 2.2. These cross-stream velocity gradients greatly affect the diffusive mixing. Near the walls, the fluid flows relatively slowly. As a result, cross-stream mixing is more pronounced in the near-wall regions, and the mixing region takes on an hour-glass shape as shown in Figure 2.1. The calculated width of the diffusive mixing region at the walls of the fuel cell is in agreement with the theoretically predicted [Ismagilov et al., (2000)] and experimentally validated [Ferrigno et al., (2002)] trend represented by the following expression:

$$\Delta x \approx \left(\frac{Dhy}{U}\right)^{1/3}$$
(2.22)

where, h is the channel height, y is the distance the fluid flows downstream, and U is the average flow speed. Down the center of the channel, the diffusive mixing region grows more slowly, following a one-half power scaling [Ismagilov et al., (2000)]. Several numerical studies have focused on the inclusion of electrokinetic phenomena in microfluidic systems [Adamczyk et al., (1999); Erickson and Li, (2002); Erickson and Li, (2003)], but due to the high ionic concentrations employed here, electrokinetic effects are negligible. The challenges in modelling microfluidic fuel

cells lie in capturing the three-dimensional mixing dynamics and the reaction and electrode kinetics.

Figure 2.3 shows a schematic of the microfluidic fuel cell with different geometries, all of which have a hydraulic diameter of 100 μm. Geometry 1 shown in Section (b) of Figure 2.3 and Geometry 2 shown in Section (c) of Figure 2.3 have electrodes placed along the top and bottom walls with a 20 μm spacing between the electrodes to account for the diffusive mixing regions. A high aspect ratio is used for Geometry 2, and a low aspect ratio is used for Geometry 3, whose electrodes are placed along the left and right walls of the channel.

Shown in Figure 2.4 are the concentration profiles of formic acid at the midpoint of the anode when the electrode kinetics were included in the model. The concentration was reduced to zero at the electrode surface, indicating that the reaction kinetics were fast compared to the diffusion in this system. This result is in keeping with experimental results [Choban et al., (2004); Ferrigno et al., (2002)]. An increase or reduction in the oxidation and reduction reaction rates also results in a diffusion limited system. Since the fuel cell is diffusion limited, the geometry of the microchannel plays a predominant role in the efficiency of the cell.

Although the fuel and oxidant streams do not experience turbulent or convective mixing, they do experience diffusive mixing. The formic acid and oxygen concentration boundary layers developed at the electrode surfaces, along with the diffusive mixing regions are illustrated in Figures 2.5 – 2.7, for Geometries 1 - 3 respectively. Section (b) in Figures 2.5 – 2.7 is the formic acid mass fraction contour plot, showing the diffusive mixing between fuel and oxidant streams at the outlet in

the absence of electro-oxidation reactions. As expected, the diffusive mixing region takes on an hour-glass shape due to the slower velocities at the walls. Section (c) in Figures 2.5 – 2.7 is the formic acid mass fraction contour plot showing the combined diffusive mixing and the electro-oxidation at the anodes. A thicker concentration boundary layer is apparent near the wall adjacent to the electrode surface and is due to the combined wall/end effects. Similarly, Section (d) in Figures 2.5 – 2.7 is the oxygen mass fraction contour plot showing the combined diffusive mixing and the electro-reduction at the cathode. Due to a constant diffusion coefficient and diffusion limited electrodes, the depletion and mixing of oxygen in Section (d) is a mirror image of the depletion and mixing of formic acid in Section (c). In each case the Reynolds number is 20, based on the hydraulic diameter, which is 100 μm in each case. A length of 6 mm downstream was chosen as the outlet in each case for comparison purposes. Fuel utilization was determined from the ratio of fuel mass flow rate at the outlet to the fuel mass flow rate at the inlet. With an inlet velocity of 0.1 m s^{-1}, the square geometry provides a fuel utilization of 3 %, whereas the rectangular geometries with aspect ratios of 1:10 provide a fuel utilization of 8 %. These results are in agreement with recent experimentally determined fuel utilizations on the order of 1 % for the square geometry presented by Choban et al. (2004) and 10 % for the rectangular geometry presented by Ferrigno et al. (2002). Although Geometry 2 and Geometry 3 provide similar fuel utilizations, there is significantly less cross-stream fuel-oxidant mixing in Geometry 2, illustrated in Section (b) of Figure 2.6. Both geometries exhibit a mixed region of similar width, but the volume of fluid in the mixed region is significantly less in Geometry 2. The degree to which

the reactants are mixed is an indication of how much potential there is for improved fuel utilization. The percentage of mixing is quantified using the following expression [Johnson et al., (2002)]:

$$\% \; mixed = \left(1 - \frac{\sqrt{\dfrac{1}{N}\sum_{i=1}^{N}\left(C_i - C_i^{mixed}\right)^2}}{\sqrt{\dfrac{1}{N}\sum_{i=1}^{N}\left(C_i^o - C_i^{mixed}\right)^2}} \right) * 100 \tag{2.23}$$

where, N is the total number of points, C_i is the concentration of point i, C_i^{mixed} is the concentration of the perfectly mixed solution at point i, and C_i^o is the concentration at point i if no mixing or diffusion were to occur. With an inlet velocity of 0.1 m s^{-1}, at the outlet of the fuel cell, Geometry 1, Geometry 2, and Geometry 3 resulted in 14 %, 8 % and 19 % mixing respectively (measured at the outlet). These results indicate that particularly for Geometry 2, there is an opportunity to utilize much more fuel.

The effect of the inlet velocity magnitude for Geometry 2 is shown in Figure 2.8. With respect to an analysis of fuel utilization and mixing, reducing the inlet velocities is effectively equivalent to increasing the length of the microfluidic fuel cell. Decreasing the inlet velocity from 0.1 m s^{-1} to 0.02 m s^{-1} causes the fuel utilization to increase non-linearly from 8 % to 23 %. This increase in fuel utilization is highly significant in the context of values provided in previous studies [Choban et al., (2004); Ferrigno et al., (2002)]. The mixing region at the outlet reached 20 μm wide, which is equivalent to the separation distance between the electrodes. Decreasing the inlet velocity further would result in fuel cross-over. It is noteworthy,

however, that the percentage mixed at the outlet increased only 3 % (from 8 % for the

0.1 m s^{-1} inlet velocity to 11 % for the 0.02 m s^{-1} inlet velocity), indicating that further

improvements in fuel utilization are possible by extending a tapered electrode beyond

the 6 mm length (while maintaining channel cross-sectional dimensions).

The schematic of Geometry 2 with extended tapered electrodes is given in

Figure 2.9. The concept is to taper the electrodes to match the growth of the mixing

region, and thereby mine unused and unmixed fuel while avoiding fuel cross-over.

With an inlet velocity of 0.02 m s^{-1}, this electrode design results in a fuel utilization

increase from 23 % to 52 %. Figure 2.10 illustrates the formic acid and oxygen

concentration boundary layers developed at the electrode surfaces, along with the

diffusive mixing regions for the extended electrode geometry. Compared to the

species mass fraction contour plots shown in Figure 2.6, where the fuel cell length

extended to only 6 mm, the contour plots shown in Figure 2.10 illustrate that the fuel

utilization has been significantly improved with the extended geometry and tapered

electrodes. Figure 2.11 illustrates the depletion of formic acid as the fuel flows

downstream. Section (a) in Figure 2.11 shows the tailored electrode placement.

Section (b) in Figure 2.11 is the formic acid mass fraction contour plot on the X-Y

plane at a depth of z = 13.75 μm (quarter plane). Section (c) in Figure 2.11 is the

formic acid mass fraction contour plot on the X-Y plane at a depth of z = 27.5 μm

(mid-plane). Due to the concentration boundary layers near the top and bottom walls

of the channel, the formic acid concentration is more depleted in the quarter plane

compared to the mid-plane. Section (c) in Figure 2.11 also shows formic acid mass

fraction contour plots at X-Z planes along the downstream channel at positions

y = 2 mm, 6 mm, 12 mm, and 18 mm. Similar to the fuel mass fraction contour in the X-Y plane, the contours in the X-Z planes also illustrate the depletion of formic acid as the fuel travels downstream.

Geometry 2 yields a total current of 0.059 mA, and when this geometry is extended with tapered electrodes the total current increases to 0.13 mA corresponding to an average current density of 1.1 mA cm^{-2}. It is noteworthy that the experimentally measured output power would be expected to be less than the theoretical prediction due to the effects associated with non-constant overpotentials and fluid properties. Furthermore, the resistivity of the fuel cell would change as the liquid flows downstream where the electrolyte concentration weakens. These results indicate that extending the length of the fuel cell geometry with tapered electrodes provides a larger total current and an improved use of reactants.

2.7   Closing Remarks

A numerical analysis of a membraneless microfluidic fuel cell was presented. The three-dimensional model accounted for the coupled flow, species transport and electrochemical reactions at the electrodes. The results show that the microchannel and electrode geometries play a significant role in the fuel utilization of the fuel cell. Extending the length of the fuel cell geometry with tapered electrodes provides a larger total current and an improved use of reactants. Simulations of the tapered-electrode microfluidic fuel cell demonstrate a fuel utilization of over 50 %.
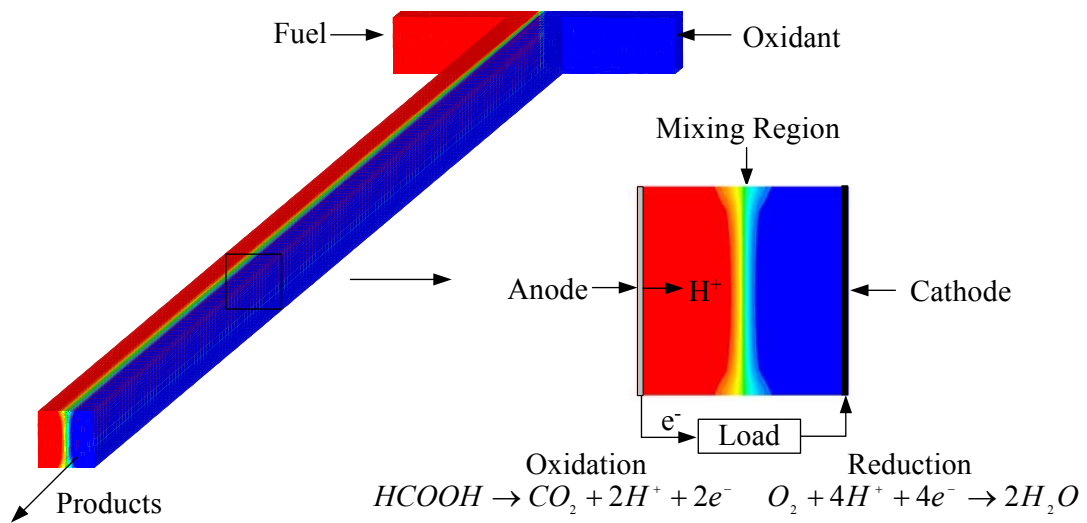
Figure 2.1. Numerical simulation and schematic of a microfluidic fuel cell with fuel and oxidant entering at separate inlets and remaining separated as they flow downstream. The flow rates and length scales were selected to illustrate the mixing process.
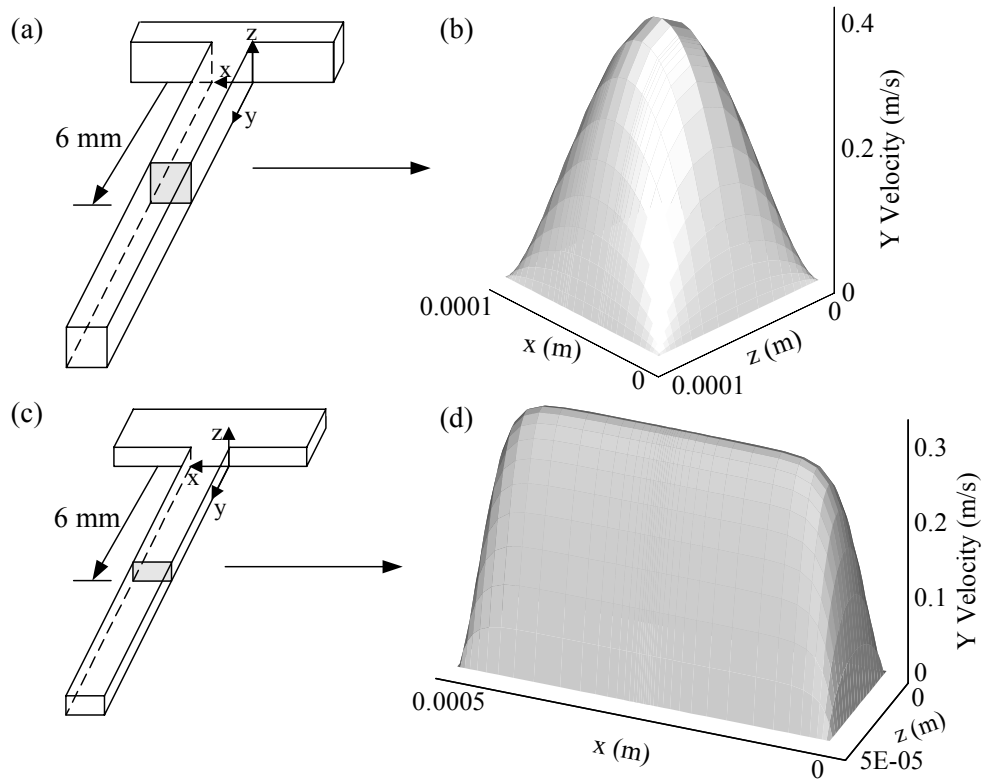
Figure 2.2. Liquid transport in the microfluidic fuel cell: (a) Schematic illustrating the location of the X-Z cross-section of interest for the axial velocity contour plot of the square geometry (100 μm x 100 μm), (b) Corresponding axial velocity contour plot, (c) Schematic illustrating the location of the X-Z cross-section of interest for the axial velocity contour plot of rectangular geometry (550 μm x 55 μm), and (d) Corresponding axial velocity contour plot.
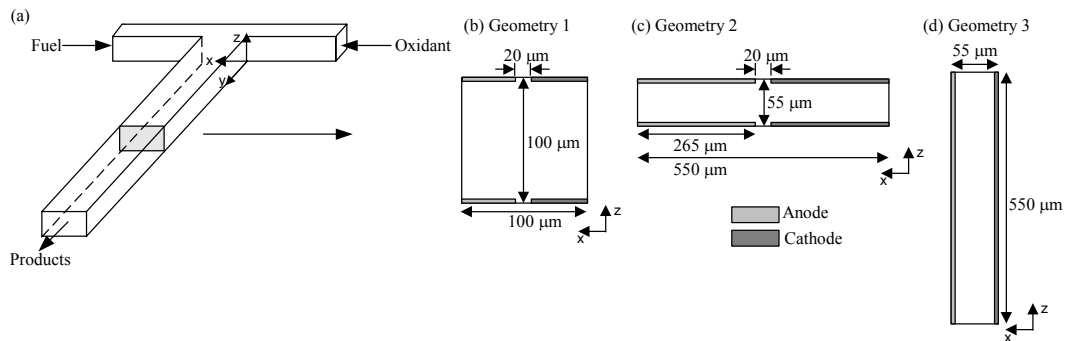
Figure 2.3. A schematic diagram of the microfluidic fuel cell system: (a) The location of the X-Z cross-section of interest, (b) Geometry 1 is square with electrodes placed on the top and bottom channel surfaces, (c) Geometry 2 is rectangular with electrodes placed on the top and bottom channel surfaces, and (d) Geometry 3 is rectangular with electrodes placed along the left and right walls of the channel.
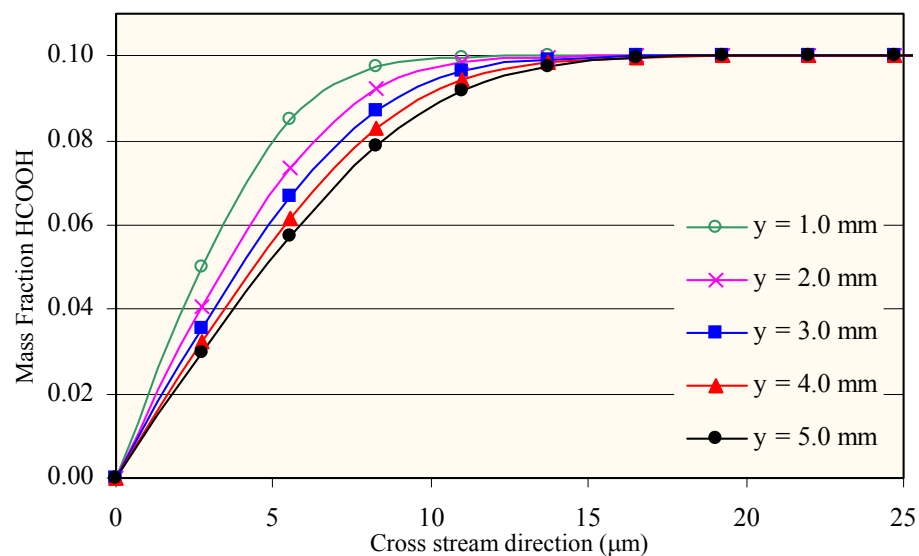
Figure 2.4. Formic acid bulk concentration normal to the anode wall for various downstream positions (at the anode midpoint). The concentration is reduced to zero at the electrode surface, indicating that the reaction kinetics are fast compared to the diffusion in this system.
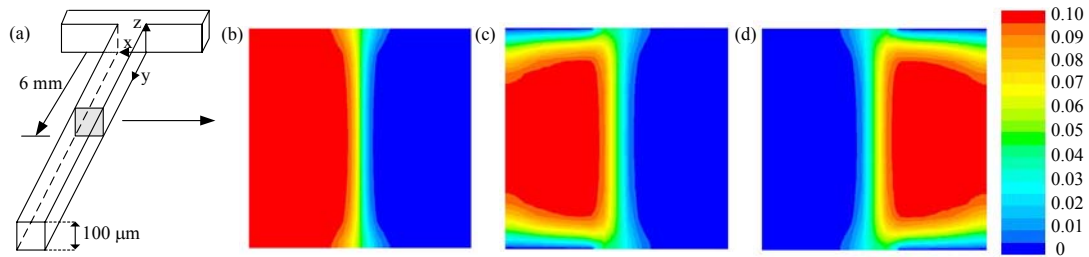
Figure 2.5. Depletion and mixing of *HCOOH* and O_2 in the microfluidic fuel cell with Geometry 1: (a) The location of the X-Z cross-section of interest, (b) *HCOOH* mass fraction contour plot showing diffusive mixing between the fuel and oxidant streams without electro-oxidation reactions, (c) *HCOOH* mass fraction contour plot showing combined diffusive mixing and electro-oxidation at the anodes (top and bottom, left), and (d) O_2 mass fraction contour plot showing combined diffusive mixing and reduction at the cathodes (top and bottom, right).
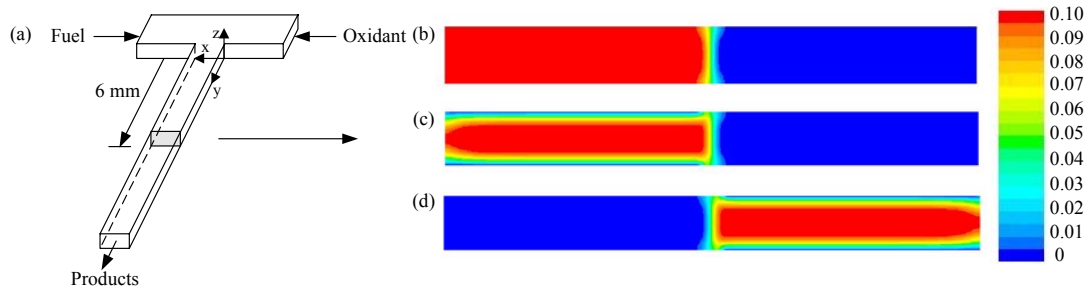
Figure 2.6. Depletion and mixing of *HCOOH* and O_2 in the microfluidic fuel cell with Geometry 2: (a) The location of the X-Z cross-section of interest, (b) *HCOOH* mass fraction contour plot showing diffusive mixing between the fuel and oxidant streams without electro-oxidation reactions, (c) *HCOOH* mass fraction contour plot showing combined diffusive mixing and electro-oxidation at the anodes (top and bottom, left), and (d) O_2 mass fraction contour plot showing combined diffusive mixing and reduction at the cathodes (top and bottom, right).
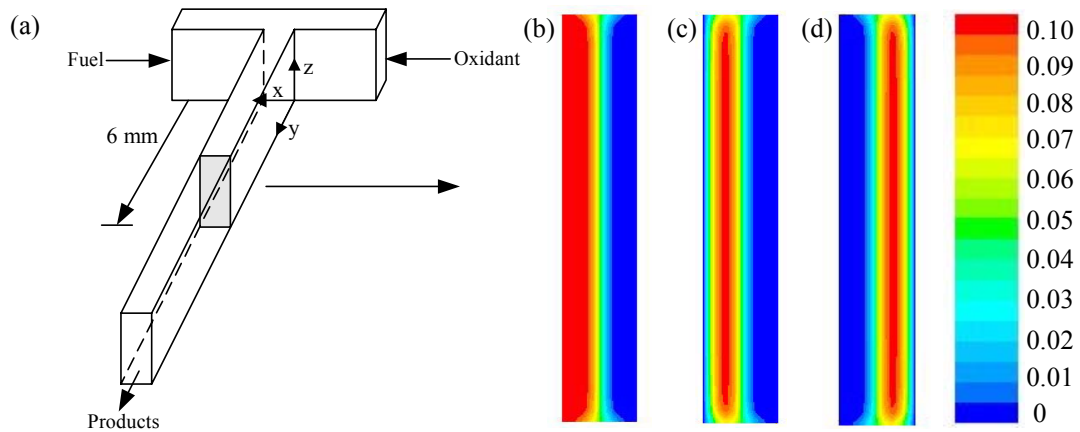
Figure 2.7. Depletion and mixing of *HCOOH* and O_2 in the microfluidic fuel cell with Geometry 3: (a) The location of the X-Z cross-section of interest, (b) *HCOOH* mass fraction contour plot showing diffusive mixing between the fuel and oxidant streams without electro-oxidation reactions, (c) *HCOOH* mass fraction contour plot showing combined diffusive mixing and electro-oxidation at the anodes (top and bottom, left), and (d) O_2 mass fraction contour plot showing combined diffusive mixing and reduction at the cathodes (top and bottom, right).
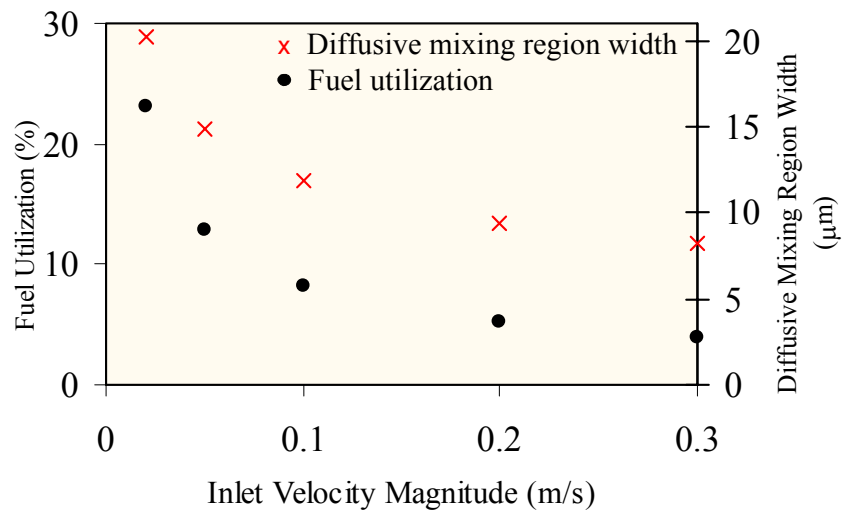
Figure 2.8. Effect of increasing the inlet velocity on fuel utilization and diffusive mixing region width for Geometry 2, measured at the outlet of a 6 mm long microfluidic fuel cell.
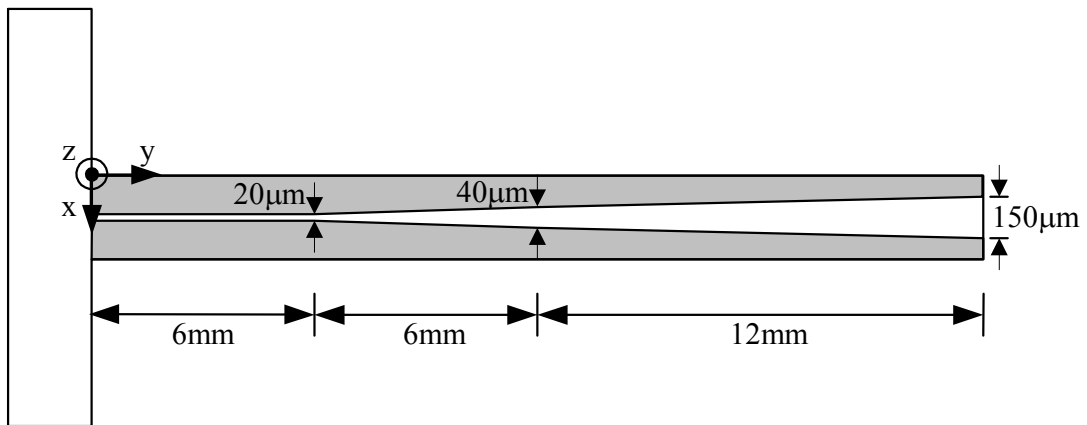
Figure 2.9. A schematic diagram of the microfluidic fuel cell system with Geometry 2 extended with tapered electrodes.
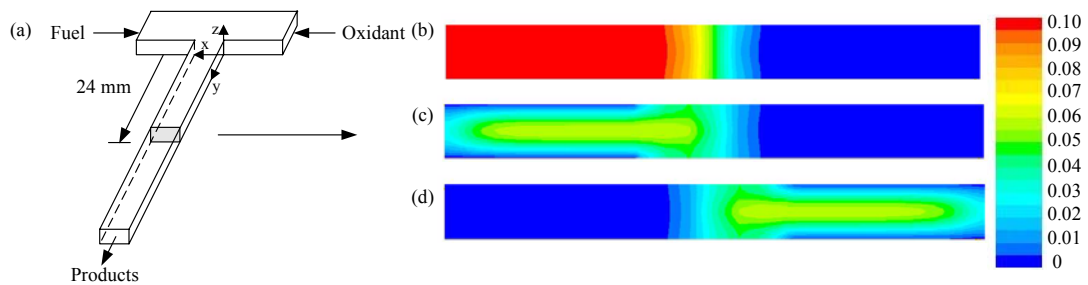
Figure 2.10. Depletion and mixing of *HCOOH* and O_2 in the microfluidic fuel cell with Geometry 2 extended with tapered electrodes: (a) The location of the X-Z cross-section of interest, (b) *HCOOH* mass fraction contour plot showing diffusive mixing between the fuel and oxidant streams without electro-oxidation reactions, (c) *HCOOH* mass fraction contour plot showing combined diffusive mixing and electro-oxidation at the anodes (top and bottom, left), and (d) O_2 mass fraction contour plot showing combined diffusive mixing and reduction at the cathodes (top and bottom, right).
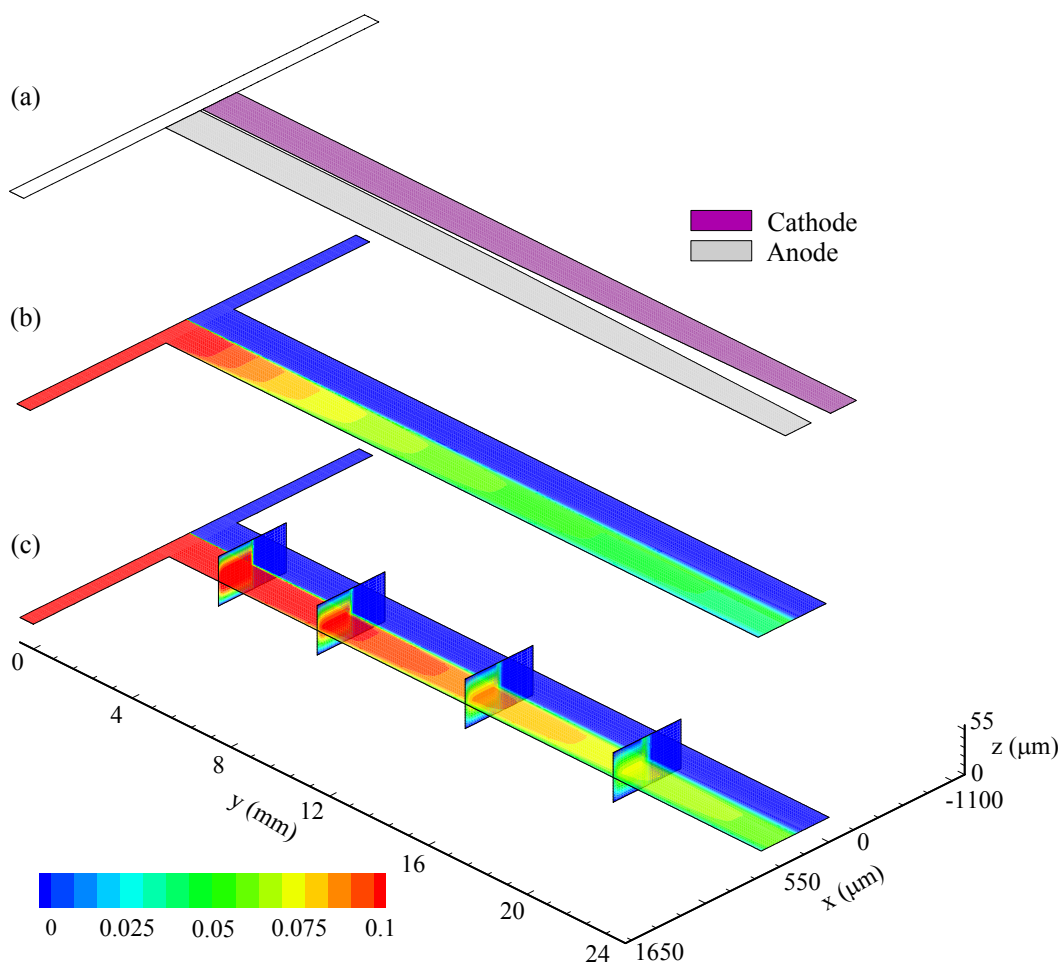
Figure 2.11. Depletion of *HCOOH* in the microfluidic fuel cell with Geometry 2 with tailored electrodes: (a) Tailored electrode placement, (b) *HCOOH* mass fraction contour plot on the X-Y plane at z = 13.75 μm (quarter plane), (c) *HCOOH* mass fraction contour plot on the X-Y plane at z = 27.5 μm (mid-plane) and at X-Z planes along the downstream channel (y = 2 mm, 6 mm, 12 mm, 18 mm). Length scales were adjusted to illustrate the depletion of *HCOOH* in the downstream direction.

Chapter 3   Distributed Heat Sources in an Enclosure

3.1   Overview

In this chapter, a computational analysis is presented of the heat transfer due to an array of distributed fuel cells modelled as flush mounted heat sources on the bottom wall of a horizontal enclosure. The parameters governing Rayleigh-Bénard natural convective flows are investigated as a method of passive heat removal. In addition to steady state simulations, a preliminary study including time dependent simulations are also performed to investigate the effects of modulating the heat flux boundary conditions of fuel cells.

3.2   Background

Natural convection provides a means to facilitate and enhance heat and mass transfer for recently developed biochemical analysis systems and microscale fuel cell designs [Krishnan et al., (2004); Lee et al., (2002); Choban et al., (2002); Ferrigno et al., (2002); O'Hayre et al., (2003); Choban et al., (2004); Hahn et al., (2004); Cohen et al., (2005); Litster et al., (2005); Bazylak et al., (2005)]. In planar fuel cells, natural convection can be used to facilitate reactant transport/exchange; however, the focus here is primarily the heat transfer characteristics. The purpose of this work is to study the effects of an infinite array of distributed fuel cells modelled as heat sources in a horizontal air filled plenum. Rayleigh numbers ranging from 0.1 to 10000 are of interest, corresponding to dry air temperature differences from 10 K to 160 K and characteristic lengths ranging from 500 μm to 10 mm.

Numerous studies have been performed on horizontal fluid layers heated from below [Rosentblat and Tanaka, (1971); Catton, (1972); Mantle et al., (1994); Soong et al., (2001); Martorell et al., (2003)]. A growing body of work also exists in the area of convection from discrete heat sources due to fundamental interests and relevance to applications in electronics [Incropera et al., (1986); Heindel et al., (1995a); Heindel et al., (1995b); Heindel et al., (1996); Ortega and Lall, (1996); Deng et al., (2002); Tou and Zhang, (2003); Bae and Hyun, (2004); da Silva et al., (2004); da Silva et al., (2005); Tso et al, (2004); Papanicolaou and Gopalakrishna, (1995)]. Incropera et al. (1986) performed experiments to determine the heat transfer due to conduction and forced convection from a four-row array of 12 heat sources flush mounted on one wall of a horizontal channel filled with water. Heindel et al. [Heindel et al., (1995a); Heindel et al., (1995b)] studied the natural convection from an array of discrete heat sources in a cavity filled with water and a dielectric fluid. They also investigated natural convection heat transfer for an array of finned, discrete heat sources in a cavity filled with a dielectric fluid [Heindel et al., (1996)]. Ortega and Lall (1996) performed experiments to measure the heat transfer coefficient on the surface of a square flush mounted heat source at the center of a plate in a small horizontal enclosure. Deng et al. (2002) presented a two-dimensional numerical investigation of natural convection from two discrete flush mounted heat sources in a horizontal enclosure with insulating sidewalls at steady state to investigate the interaction between sources. Tou and Zhang (2003) presented a three-dimensional numerical model to investigate the heat transport in a liquid-filled vertical rectangular enclosure with a 3 x 3 array of discrete flush mounted heaters along one vertical wall. The

opposite wall acted as a uniform cold surface, and all other walls were insulating. Bae and Hyun (2004) studied two-dimensional laminar natural convective air-cooling in a vertical rectangular enclosure with three discrete flush mounted heaters on one side of the wall. The thermal condition of the lowest-elevation heater alternated between 'on' and 'off', and the resulting effect on transient heat transfer for the other sources was studied. Da Silva et al. (2004) investigated the optimum distribution of heat sources cooled by laminar natural convection for a small number of heat sources mounted on the sidewall of an enclosure and for a large number of heat sources mounted on a vertical wall facing a fluid reservoir. Da Silva et al. (2005) also investigated the optimal distribution and sizes of three discrete heat sources in a vertical open channel cooled by natural convection. Tso et al. (2004) presented experimental and numerical results for the laminar natural convection cooling of water in a rectangular cavity with a 3 x 3 array of heaters on one wall at various angles of inclination. Papanicolaou and Gopalakrishna (1995) presented a two-dimensional computational investigation of natural convection in a shallow horizontal air layer driven by a single flush mounted discrete constant heat flux source. They investigated the parameters governing the transition from the conduction-dominated regime to a convection-dominated regime. The geometric parameters studied in their work are the width-to-height aspect ratio of the air layer to the uniformly heated source length. With a uniform heat source, a discrete transition region was observed, whereas with discrete heating, the transition was continuous. For each source length, an optimum aspect ratio for heat transfer was found. In the presence of three discrete heat sources, they found that the transition from conduction to convection was significantly delayed in the presence of adjacent

sources compared to the single source; however, the rate of increase of Nusselt number with increasing Rayleigh number was higher in the case of multiple heat sources.

All previous works focused on a finite number of heat sources; however with the trend towards electronic miniaturization and increasing component density, the number of components asymptotically approaches an infinite value. The design of more efficient passive cooling for high density packaging of electronic devices requires a better understanding of the parameters governing natural convective heat transfer in the basic arrangement of a horizontal enclosure with many discrete heat sources. This work provides new insight on the physical parameters, such as source length and spacing, which control the onset and generation of sustained natural convection in a horizontal air layer with a large number of heat generating components. Specifically, the limiting case of an infinite array of distributed heat sources is simulated with the use of periodic boundary conditions. The effects of source spacing and source length on heat transfer rates and flow regimes are determined, and the impact of using periodic boundary conditions in modelling these flows is discussed.

3.3   Mathematical Model

Figure 3.1 illustrates the geometric and thermal boundary conditions of the two-dimensional problem under consideration. Temperature contours for the conduction-dominated regime for this configuration are also shown in Figure 3.1. Flush-mounted heat sources of equal length, L, have prescribed uniform heat flux

boundary conditions, q_L". The heat sources are separated by length, S, and the height of the plenum is H.

The following conditions are prescribed on the other boundaries:

- bottom wall, between sources: zero heat flux boundary condition, q_S" $= 0$;

- top wall: constant temperature, T_L;

- bottom and top walls: no-slip velocity condition;

- side boundaries: periodic boundary condition.

The periodicity condition simulates an effectively infinite array of heat sources without the influence of sidewalls. Having a sufficiently large computational domain between periodic boundary conditions is of critical importance to the numerical results in order to avoid constraining the wavelength of the convection patterns. In some cases, the computational domain size requirements change after transition from one regime to another, which will be discussed further. In this work, the maximum temperature difference, ΔT, is assumed small enough to justify the use of the Boussinesq approximation, which assumes a variable density in the buoyancy force of the momentum equation in an otherwise incompressible fluid. The resulting continuity, momentum and energy equations governing the flow and heat transfer are given by:

$$\nabla \cdot \vec{v} = 0 \tag{3.1}$$

$$\frac{\partial \vec{v}}{\partial t} + \nabla \cdot \left(\vec{v}\vec{v} \right) = -\frac{1}{\rho} \nabla P + \nabla \cdot \left(\upsilon \nabla \vec{v} \right) + \beta \, \Delta T \, \vec{g} \tag{3.2}$$

where, $\vec{v}$ is the velocity vector, t is the time, ρ is the fluid density, P is the static pressure, υ is the kinematic viscosity, β is the thermal expansion coefficient, and $\vec{g}$ is the acceleration of gravity.

$$\rho C_p \left(\frac{\partial T}{\partial t} + \vec{v} \cdot \nabla T \right) = k^* \nabla^2 T \qquad (3.3)$$

where, C_p is the specific heat capacity, k^* is the thermal conductivity and T is the temperature.

The heat transfer from the sources is expressed in terms of the Nusselt number averaged over the area of the source, which is defined as:

$$Nu = \frac{h^* H}{k^*} \qquad (3.4)$$

where, H is the characteristic length of the system, and h^*, the heat transfer coefficient is defined as,

$$h^*(x,t) = \frac{q''(t)}{T_S(x,t) - T_L} \qquad (3.5)$$

For time dependent simulations, the temporally-averaged and spatially-averaged Nusselt number is given by:

$$Nu_{avg} = \frac{1}{\tau}\int\limits_0^\tau \frac{1}{L}\int\limits_0^L Nu(x,t)\,dxdt \tag{3.6}$$

where, τ is the period of oscillation. There are several length parameters associated with this geometry, such as the plenum height, H, heat source length, L, and spacing, S. The characteristic length of the system is defined here as the plenum height, H, which greatly impacts the Rayleigh-Bénard cell structure and pattern. The Rayleigh number is defined as:

$$Ra = \frac{g\beta\left(T_{max} - T_L\right)H^3}{\alpha^* \nu} \tag{3.7}$$

where, T_{max} is the maximum temperature on the surface of heat source, and α^* is the thermal diffusivity of air. For evenly spaced distributed heat sources the ratio of source length to plenum height (L/H) is also an important parameter. For materials with low emissivity, radiation is not a significant heat transfer mechanism and is neglected throughout this investigation. Although the results have been non-dimensionalized to apply to any length scale, in the context of the air properties and temperature differences of interest, the length scale ranges from 500 μm to 10 mm. The Prandtl number has a value of 0.74 and is given by,

$$Pr = \frac{\nu}{\alpha^*} \tag{3.8}$$

This model was implemented in Fluent, a commercial finite-volume based CFD package. The governing equations and the prescribed boundary conditions were discretized with a QUICK scheme [Fluent 6.1.22]. For steady state simulations PRESTO was used, and for time dependent simulations PISO was used as the descretization method for pressure [Fluent 6.1.22]. The SIMPLE method was employed for the pressure-velocity coupling scheme, and a slightly stretched hexagonal grid and a segregated solver were used for all simulations. For the time dependent calculations, a second order implicit formulation was used with constant time steps of 10^{-2} s.

3.4   Steady State Convection-Diffusion Results

In an infinite horizontal layer being heated from below, the theoretical critical Rayleigh number is 1708 [Incropera and De Witt, (1990)]. Soong et al. (2001) found that the presence of confining sidewalls results in a higher critical Rayleigh number, and Papanicolaou and Gopalakrishna (1995) reported that for a discrete heat source with confining sidewalls, there is a range of critical Rayleigh numbers, depending on the length of the source and height of the domain. In this paper, the constraint of the sidewalls is removed, effectively considering an infinite array of distributed heat sources and their effects on heat transfer. Along with the trend of increasing electronic miniaturization, there is also a trend towards increasing component density. As the number of electronic components increases and plenum height decreases, the end effects become much less significant, and the spacing between the components

becomes the dominant parameter. The geometry and periodicity considered here are thus good representations of such conditions.

3.4.1 Source Spacing

The effect of source spacing was investigated with the geometry shown in Figure 3.1 at steady state with uniform and equal heat flux boundary conditions for each heat source. In Figure 3.2 the source length, L, and plenum height, H, are equivalent ($L = H$) and this one-to-one ratio is held constant. The Rayleigh number (Ra) is increased to study the effects on the average Nusselt number (Nu) when the dimensionless spacing length between the sources, S/L, is varied.

Figure 3.2 (a) shows that Nu begins to plateau for $S/L > 1$. Heat transfer is not maximized for shorter spacing lengths, and there are no dramatic benefits to increasing the spacing length further. It is also noteworthy that larger separation lengths are not desirable in the applications of interest. The maximum velocity (V_{max}) versus Ra for various spacing lengths is plotted in Figure 3.2 (b), where the rate at which V_{max} increases with increasing Ra also reaches a ceiling for non-dimensional spacing lengths greater than $S/L = 1$. Papanicolaou and Gopalakrishna (1995) used a spacing of 0.5 times the length of the source to ensure significant interaction between three heat sources. Considering the results shown in Figure 3.2 and the simplicity of the $S = L$ configuration, this source pattern is utilized in all following computations.

Figure 3.3 shows typical temperature and convection patterns in the convection-dominated regime for the horizontal fluid layer heated from below by distributed heat sources where $S = L = H$. The temperature contours in Figure 3.3 (a)

show the thermal plumes that develop above each heat source. The velocity streamfunctions shown in Figure 3.3 (b) show the development of Rayleigh-Bénard convection cell pairs above each heat source. Figure 3.3 (c) and (d) show the velocity vectors associated with the cell structures. Buoyancy forces induce the heated fluid at the source to rise vertically towards the upper cooled surface. The temperature of the fluid cools as it reaches the upper surface and is driven downwards, where its temperature begins to rise again due to the heat source. The $S = L = H$ configuration leads to the stable repeating pattern of roughly-circular circulations centered on the edges of each source.

3.4.2   Source Length

In the following simulations, the source length and the spacing length are equal ($S = L$). This ratio is kept constant, while Ra is increased by varying L. The average Nu versus Ra is plotted in Figure 3.4 for various ratios of source length to plenum height, L/H. Figure 3.4 shows the effect on heat transfer when increasing the length of the heat sources. In agreement with Tso et al. (2004), the transition from a conduction-dominated regime to a convection-dominated regime occurs in the elbow region of the average Nu versus Ra plot. Papanicolaou and Gopalakrishna (1995) found that with three discrete heat sources, flow transitioned to the convection-dominated regime above the middle source at $Ra = 2347$ and above the side sources at $Ra = 1509$. The flow above the side sources experienced a relatively earlier transition due to the effects of confining sidewalls. Here, the transition region is found to occur in the range $500 < Ra < 2000$, for source lengths between $L = 0.1H$ to

$L = 1.8H$, and the transition occurs at the same Ra for all sources since there are no confining sidewalls. As the source length increases, the transition begins at smaller Ra and grows slowly with Ra. As the source length decreases, the transition region becomes sharper, approaching the solution for the classical bottom wall heating solution reported by Papanicolaou and Gopalakrishna (1995). In the conduction-dominated regime, the average Nu decreases as the source length relative to the plenum height increases. The rate of increase of the average Nu decreases as the source length increases in the convection-dominated regime. In the convection-dominated regime, Nu increases steadily with Ra, with the $L = 0.1H$ source length configuration showing the best rate of heat transfer. The $L = 0.6H$ source length configuration shows an irregularity between $Ra = 5800$ and $Ra = 8100$, which will be revisited later.

Figure 3.5 shows V_{max} versus Ra for various source lengths, and similar to the curves shown in Figure 3.4, the transition region occurs where $Ra \sim 1000$. The maximum velocity increases at a faster rate as Ra increases for longer source lengths. In Figure 3.5 a higher V_{max} occurs in the transition region for increasing source lengths. In the convection-dominated regime, well beyond the transition region, V_{max} for varying source lengths approach the same values and increase at the same rate.

For the cases with relatively short source lengths, the Rayleigh-Bénard cells undergo significant growth in the transition region. For the source length of $L = 0.1H$, weak cell pairs are observed over each heat source in the conduction-dominated regime as shown in Figure 3.6 (a). For the same geometry in the convection-

dominated regime, stronger cell pairs develop over a number of heat sources, as shown in Figure 3.6 (b). The transition region occurs between Ra = 980 and Ra = 1560 for this source length configuration, as shown in Figure 3.4. The radical change in Rayleigh-Bénard cell structure accounts for a sharper transition and high heat transfer rates in the convection-dominated regime, compared to configurations of longer heat sources. With the larger and stronger convection cells present, heat transfer is improved. For configurations with source length and plenum height closer to a one-to-one ratio, the weak Rayleigh-Bénard cell structure that appears in the conduction-dominated regime remains similar in the convection-dominated regime. Without an abrupt change in Rayleigh-Bénard cell structure, the heat transfer rates are significantly lower than for the L = 0.1H configuration. With respect to modelling these flows, it is noteworthy that the domain size requirement greatly increases following the transition to the convection-dominated regime. The domain shown in Figure 3.6 (a) is sufficient to ensure domain size independent solutions in the conduction-dominated regime. Following the transition, however, only two cells fill this same area. To avoid artificial forcing of the solution to specific cell patterns or wavelengths, a sufficiently large computational domain must be used for all simulations near the transition region (as shown Figure 3.6 (b) inset).

For the case where L = 0.4H, bifurcations were observed for Ra beyond 2900, which occurs well within the convection-dominated regime. Depending on the size of the domain, the structure of the Rayleigh-Bénard cells changes and cells develop over multiple heat sources. Figure 3.7 illustrates the bifurcation observed for this configuration where the Ra = 3660 and the number of heat sources in the domain is

10, 15 and 20 in Figure 3.7 (a), (b) and (c) respectively. The nonuniqueness of the solution is an inherent physical and numerical feature of Rayleigh-Bénard flows [Nikfetrat et al., (1995)]. Heat transfer coefficients and maximum velocities do not vary significantly for the solutions obtained at this Ra in Figure 3.7 (a), (b), and (c). It is important to note that other solutions generating different flow patterns may be possible depending on physical or numerical perturbations [Nikfetrat et al., (1995)].

For the case where $L = 0.6H$, a bifurcation associated with a regime change is observed for $5800 < Ra < 8100$, well within the convection-dominated regime. This bifurcation is accompanied by an abrupt decrease in Nu, as shown in Figure 3.8. This is in contrast to the coalescence of cells observed at transition for smaller source lengths, which resulted in an increased rate of heat transfer, as shown in Figure 3.6. The average Nu decreases from 4.0 to 3.6 when Ra changes from 5800 to 8100. The maximum velocity does not experience any abrupt changes in this Ra region, but the thermal plumes change from developing over a pair of heat sources at $Ra = 5800$ to a plume developing over each heat source at $Ra = 8100$, as shown in Figure 3.8 (a) and (b), respectively. Due to the non-linearity of the Rayleigh-Bénard problem, degeneracy of this nature is possible and similar phenomena have been observed in other natural convection flow situations [Nikfetrat et al., (1995); Bahloul et al., (2004); D'Orazio et al., (2004)]. Nikfetrat et al. (1995) investigated the machine and mesh sensitivity and the effect of initial perturbations on the onset and development of natural convection in fluids. They noted that the problem is characterized by non-unique solutions, and that the specific numerical realization that is obtained depends on the numerical noise, which causes uncontrolled perturbations. They suggested that

when the perturbation applied to the actual physical process is well characterized, a similar numerical perturbation should be applied to the simulation to match this situation. Bahloul et al. (2004) also observed Rayleigh-Bénard bifurcation in the numerical solution of natural convection in a vertical porous slot heated from below. D'Orazio et al. (2004) presented a two-dimensional natural convection problem in a tall vertical rectangular enclosure heated from below and cooled from above. Bifurcations were observed in the convection-dominated regime, which resulted in both smooth and abrupt changes in *Nu*. This work is the first report of bifurcations associated with a large array of discrete heat sources in a horizontal air plenum that lead to significant heat transfer reductions.

3.5   Thermal Radiation

3.5.1   Thermal Radiation Background

For the cases where high temperature values are expected, thermal radiation has been included in the model to investigate the individual effects of all three modes of heat transfer. Thermal radiation is the emission of energy in the form of electromagnetic waves by matter due to the vibrational and rotational motions of atoms or molecules. When considering thermal radiation, the spectral distribution and the magnitude of each wavelength are dependent on the temperature and the material properties of the radiating surface. A radiating surface may also emit electromagnetic waves preferentially in certain directions, which causes a directional distribution of radiation emissions. Emissivity is generally constant for conductors over the range $\theta \leq 40°$ ($\theta = 0°$ represents the surface normal), after which it increases with θ, and

eventually decays to zero. Emissivity is constant for nonconductors for $\theta \leq 70°$ after which it decreases to zero. When considering directional distribution, the hemispherical emissivity, ε, of a differential area element differs only slightly from the emissivity normal to the surface, ε_n. Typically, the ratio lies within the range $1.0 \leq \varepsilon/\varepsilon_n \leq 1.3$ for conductors and $0.95 \leq \varepsilon/\varepsilon_n \leq 1.0$ for nonconductors. Therefore, it is reasonable to neglect the directional distribution of emission and assume that the surface is a diffuse emitter, i.e., the emissivity is independent of direction and $\varepsilon = \varepsilon_n$ [Incropera, (1990)].

Fuel cells can be integrated into large arrays similar to integrated circuit boards in electronics. In electronics, computer processor units generate the most heat compared to other components on an electronic printed circuit board. Processors are generally equipped with layers of materials to help conduct the heat away from the chip and exposed to a fan to advect the heat away. Electronic components that do not generate any significant amounts of heat are generally placed inside plastic casings. For components that generate enough heat that it is worthwhile to provide a heat sink, aluminum is very commonly used. Heat sinks vary from being a flat piece of metal connected to the component to conduct the heat away to more elaborate pin-fin heat sinks with a variety of profiles.

Generally speaking, metallic surfaces such as highly polished silver and gold have small emissivities as low as 0.02. Oxide layers on metallic surfaces significantly increase the emissivity of the surface. For lightly oxidized stainless steel, the emissivity is about 0.10, and for heavily oxidized stainless steel, the emissivity is approximately 0.50. Nonconductors have emissivities that generally exceed 0.60. The

emissivity of aluminum can range from 0.05 for a highly polished surface to 0.95 for anodized finishes [Incropera, (1990)]. Other metals used to dissipate heat on electronic printed circuit boards include copper and brass, although they are not as common as aluminum because they are more expensive. Absorptivity, α_{abs}, is a material property that determines the fraction of the irradiation that is absorbed by a surface, and just like emissivity, absorptivity is also directionally and spectrally dependent. It is often reasonable to assume that the dependence of absorptivity on surface temperature can be neglected [Incropera, (1990)].

A gray surface is a surface with equal emissivity and absorptivity, i.e., $\varepsilon = \alpha_{abs}$. Wavelength dependent emissivity and absorptivity are equal ($\varepsilon_\lambda = \alpha_{abs,\lambda}$) if either of the following conditions is satisfied:

a) the irradiation is diffuse, which means that the intensity of radiation upon a surface is directionally independent, or

b) the surface is diffuse, which means that the emissivity and the absorptivity are directionally independent.

Condition b) is a good approximation for electrically non-conducting materials [Incropera, (1990)]. The hemispherical emissivity, ε, is equal to the hemispherical absorptivity, α, if either of the following conditions is satisfied:

a) the irradiation on a surface is due to blackbody radiation, or

b) the surface is gray, and ε and α_{abs} are independent of wavelength, λ.

So, in general, a gray surface refers to a surface that is direction and wavelength independent with respect to both emissivity and absorptivity. This approximation is a reasonable assumption for many engineering applications [Incropera, (1990)].

Kulkarni and Das (2005) presented thermal models for cooling microscale electronic processor chips through forced and natural convection. They based the radiation heat transfer from the sink using an emissivity of 0.07. Since there has been a dramatic increase in chip density and power density along with the trend towards miniaturization, thermal management is the most critical area of electronics development. Kulkarni and Das (2005) developed heat sinks for small chips on the order of a few micrometers in size, called Nanoblocks. A company called Alien Technology recently presented Nanoblocks, which are 600 μm x 600 μm in size and dissipate 5 mW of thermal power, at the University of Alaska Fairbanks. These authors designed the heat sink using pure aluminum. They found that it took 18 ms for the temperature of the chip and heat sink to reach steady state. To increase the radiative heat dissipation, paints of high emissivity materials were used with an emissivity of 0.9.

Hanreich et al. (2000) presented a thermal simulation tool based on the alternating direction implicit method. They noted that in 1990, a microprocessor dissipated no more than 3 W of heat on a chip with a size of 1 cm^2, but in the year that this article was written (2000) Pentium processors produced power losses of up to 50 W on a chip with a size of 2 cm^2, which is equivalent to a heat flux of 2.5×10^5 W m^{-2}. According to Sartre and Lallemand (2001), computer chips reached heat fluxes of the magnitude 100 W cm^{-2}. The emissivity of the thermal test die casing they used was determined to be 0.89. Since the emissivity of materials varies significantly depending on the surface characteristics, an intermediate emissivity

value of 0.5 will be used for simulations to show the effects of radiation for a general surface.

3.5.2   Thermal Radiation Results

For all simulations, we assume that the medium, which is air, is non-participating. This means that the medium neither absorbs nor scatters surface radiation and emits no radiation, which is a good assumption for diatomic gases such as O_2 and N_2 [Incropera, (1990)]. This is not true for larger molecules such as CO_2, H_2O and hydrocarbon gases, which emit and absorb radiation over a large temperature range [Incropera, (1990)]. This assumption can be used for the simulations with air, but this assumption may no longer be valid for reactant species involved in fuel cell reactions. The index of refraction of air at 0 ºC is $n_r = 1.000293$ measured with light of vacuum wavelength $\lambda_o = 589\ nm$ [Serway, (1983)]. For all simulations, it is assumed that the index of refraction is constant over all wavelengths and temperatures.

The following simulations were done for the configuration where $L = H = S$ with the assumptions discussed above. The following curves in Figure 3.9 and Figure 3.10 show the effect of modelling blackbody radiation ($\varepsilon = 1$). When only convection and conduction are modelled, the critical Ra is approximately 810, which corresponds to a characteristic length of $L = H = S = 4$ mm given a temperature difference of 116 K. This is the point at which convection begins to be the dominant heat transfer mode. When all three modes of heat transfer are simulated, the critical Ra is approximately 1220, which corresponds to a characteristic length of $L = H = S =$

5.5 mm given a temperature difference of 65 K. It is important to note that increasing thermal radiation delays the onset of thermal instability in the system. Nu increases with increasing emissivity, and the intermediate value for emissivity ($\varepsilon = 0.5$) produces a curve, which lies between that of no radiation and blackbody radiation.

When radiation is also simulated, the transition becomes smoother, and as expected, the heat transfer rates are significantly higher. However, V_{max} is less in the cases with radiation compared to the cases without radiation in the convection-dominated regime, as shown in Figure 3.10. Figure 3.10 also shows that as the emissivity increases from $\varepsilon = 0$ (no radiation) to $\varepsilon = 1$ (Blackbody radiation), V_{max} shows a decreasing trend. However, it is important to note that V_{max} does not significantly decrease with increasing Ra. This is a promising result because it indicates that high emissivity surfaces can be used to help remove heat from the surfaces of fuel cells without sacrificing the strength of the Rayleigh-Bénard convection cells that are advantageous for enhancing reactant mass transfer. Figure 3.11 is a plot of maximum $\varDelta T$ versus Ra for the $L = H = S$ configuration. As emissivity and absorptivity increase, the maximum $\varDelta T$ significantly decreases, especially in the convection-dominated regime.

3.6   Heat Flux Modulation

3.6.1   Heat Flux Modulation Background

Unsteady heat generation is common in electronic components, and more importantly, small-scale systems can be designed to induce dynamic heat fluxes. The focus of this study is the enhancement of natural convection based heat transfer

through independent modulation of heat fluxes from a planar array of distributed fuel cells.

Many studies have been performed on horizontal fluid layers heated from below with oscillating temperature boundary conditions. Rosentblat and Tanaka (1971) conducted an analytical study using the Boussinesq approximation of the thermal convection in a situation where an incompressible fluid is confined between two parallel, horizontal and rigid planes that extend infinitely in the horizontal direction. They investigated the effect of modulating the temperature gradient, and they found that bottom wall temperature modulations of high amplitude and low frequency delayed the onset of instability in the flow field. Specifically, they investigated the effects of frequency and amplitude on the critical Rayleigh number. Low frequency modulation and high amplitude modulation produced higher critical Rayleigh numbers. The top wall had a zero temperature boundary condition, and the bottom wall had a temperature boundary condition that oscillated sinusoidally about a positive mean value.

Mantel et al. (1994) investigated the effects of temperature modulation on natural convection in a horizontal water layer heated from below. Experiments were performed in which the bottom wall temperature varied in a "sawtoothlike" fashion, and the period of oscillation ranged from 43 s to 93 min. The flow was turbulent for all cases, and the effects on heat transfer were studied at high Rayleigh numbers. They studied the period and amplitude of oscillation as well as the Rayleigh number and found that the enhancement in heat transfer is largely affected by the amplitude and period of temperature oscillation. With small changes in the bottom wall

temperature (less than 15 %), the average heat transfer does not significantly change from the well-established steady-state value. For large temperature modulations of greater than 30 %, the cycle-average heat transfer increases to 12 % compared to the steady state value. The period of oscillation has no effect on the heat transfer rates when the amplitude of fluctuation is small, but the period has a large effect when the amplitude of fluctuation is large.

Soong et al. (2001) provided a two-dimensional numerical study of bottom-wall temperature modulation effects on thermal instability and cellular convection in a rectangular enclosure. In their study, a rectangular enclosure was heated from below with a wall temperature that varied sinusoidally with time. Soong et al. (2001) found that a bottom-wall temperature modulation of larger amplitude and lower frequency induces a stabilizing effect, in agreement with previous work by Rosentblat and Tanaka (1971). The Boussinesq approximation was assumed, and the critical Rayleigh number at which the stationary conduction state changed to a cellular convection one was found to be higher than the theoretical Rayleigh number of 1708 for an infinite fluid layer heated from below. The authors attributed this to the stabilizing effect of sidewall confinement.

Bae et al. (2004) presented a time dependent two-dimensional numerical study on laminar natural convection air-cooling in a vertical rectangular enclosure with discrete flush mounted heaters on one side of the wall. Three heaters were situated on the sidewall, and the lowest elevated source was switched 'on' and 'off', while the others were kept 'on'. Numerical simulations were conducted for Rayleigh numbers between 10^5 and 10^7, and the authors used the Boussinesq approximation. According

to the authors, a discretely heated vertical wall leads to a higher heat transfer coefficient than a fully heated vertical wall, which was shown by other authors [Keyhani et al., (1988)]. The lower elevation heater has a large influence on the higher-elevation heaters due to the interactions of the thermal wake of the lower one. The purpose of switching the lower heater 'on' or 'off' is to show that the transient temperatures of the other heaters may get higher at unsteady modes compared to steady state. In one case, the lower elevated source is switched 'on' and 'off' periodically.

Shu et al. (2005) presented experimental and numerical investigations on natural convection in a cavity with oscillating wall temperatures. Numerical simulations were used to study the effects on modulation frequency and Prandtl number on the fluid flow. The authors considered a rectangular cavity with adiabatic top and bottom surfaces, which was filled with distilled water. The right side was kept at a constant temperature, and the left side had a sinusoidally oscillating temperature boundary condition. The boussinesq approximation was used, and a finite element method was applied. They found that the flow oscillation in the cavity strongly depends on the frequency of temperature perturbation applied to the boundary, where the flow modulation is weaker at high frequencies of temperature oscillation. They also found that for low Prandtl number fluids, the temperature and gravity oscillations produce similar effects on flow patterns and temperature distributions within the cavity.

Roppo et al. (1984) presented an analytical study of Rayleigh-Bénard convection in a thin liquid layer heated from below, where the lower boundary is

modulated sinusoidally in time. The horizontal layer of Boussinesq fluid extended infinitely in the horizontal direction between two parallel planes. The top wall was kept at a constant lower temperature, and the lower plate oscillated sinusoidally about a nonzero mean value.

Tang and Bau (1998) numerically investigated Rayleigh-Bernard convective flow patterns in a fluid layer confined in a cylinder heated from below and cooled from above. They used a feedback control system with multiple sensors and actuators to stabilize the conductive state and to postpone the transition to a convective state.

The purpose of this work is to investigate the effects on heat transfer when the heat flux boundary conditions for a large array of integrated fuel cells are modulated with respect to time.

3.6.2   Heat Flux Modulation Results Including Thermal Radiation Effects

The effects of source heat flux modulation on heat transfer rates are studied for the case where $\varepsilon = 0.5$ and $L = S = H = 6$ mm with a temperature difference of $\Delta T = 90$ K, which corresponds to $Ra = 1560$. This operating point occurs within the convection-dominated regime, as shown in Figure 3.9. As in previous simulations, the heat flux boundary conditions stipulate a uniform heat flux profile along each heat source. In the following investigation, all heat sources are modulated by the same frequency, ω, with constant time steps of 10^{-2} s. The period of oscillation is 1.5 s, which was determined from a transient simulation used to see how much time was required for this system to reach steady state. This was the minimum time for the system to reach steady state. As shown in Figure 3.12, a shorter time period results in

oscillating a system too quickly for the system to develop a quasi-steady state condition. Figure 3.12 shows Nu, V_{max}, ΔT and Ra rising to steady state values after approximately 1.5 s.

The heat flux boundary conditions for each heat source are modulated sinusoidally, and alternating heat sources are phase shifted by an angle, ϕ. Where B is the mean value about which the heat sources are modulated, the heat fluxes of alternating sources are given by:

$$q''_{lag} = B[1 + \delta \sin(\omega\, t)] \tag{3.9}$$

$$q''_{lead} = B[1 + \delta \sin(\omega\, t + \phi)] \tag{3.10}$$

Figure 3.13 shows the effects on heat transfer when the oscillation amplitude, δ, of the heat flux modulation was varied from 0 to 1. Figure 3.13 (a) shows the heat flux boundary condition of each heat source over one period. Figure 3.13 (b) shows Nu over one period, Figure 3.13 (c) shows the temperature difference between the cold upper wall and the average source temperature, and Figure 3.13 (d) shows the maximum velocity. As shown in Table 3.1, compared to the steady state case where $\delta = 0.0$, over one period of time, average values of Nu_{avg}, V_{max} and Ra decrease with increasing value of oscillation amplitude. On the other hand, the temperature difference between the cold upper wall and the average source temperature decreases. This decrease in temperature difference shows an improvement in heat transfer from the heat sources.

Compared to the steady state case where $\phi = 0°$, Nu_{avg} decreases by approximately 10 % when a phase shift is introduced. This is shown in Figure 3.14 and in Table 3.2. Even though Nu_{avg} decreases, the temperature difference between the cold upper wall and the average source temperature decreases by almost 6 % with phase shifted heat sources. At first glance, Nu_{avg} may be expected to increase with a decrease in temperature difference, which is valid in a steady state situation. Here, this is an incorrect assumption because Nu_{avg} is averaged with respect to space and time. Recall the expression for the temporally-averaged and spatially-averaged Nusselt number, which is given by:

$$Nu_{avg} = \frac{1}{\tau}\int_0^\tau \frac{1}{L}\int_0^L Nu(x,t)\,dx\,dt \qquad (3.11)$$

Over one period of time, the average maximum velocity, $V_{max,avg}$, increases by about 41 % when the heat sources are out of phase by 180°. Even though Ra and Nu_{avg} decrease when phase shifted heat sources are introduced, it is important to note that a decrease in temperature difference is observed, and an increase in $V_{max,avg}$ is observed, both of which are desirable for heat removal and enhanced reactant transport in the fuel cell design.

3.7 Closing Remarks

In this chapter, a computational analysis is presented of the heat transfer due to an array of distributed fuel cells modelled as flush mounted heat sources on the bottom wall of a horizontal enclosure. The parameters governing Rayleigh-Bénard

natural convective flows are investigated as a method of passive heat removal. Using steady state simulations, a fuel cell spacing length equal to the fuel cell length is found to provide effective convective heat transfer, and fuel cell lengths that are short with respect to the plenum height provide the best rates of heat transfer. In addition to steady state simulations, a study including time dependent simulations performed to investigate the effects of modulating the heat flux boundary conditions of fuel cells shows an improvement in heat and mass transfer through decreases in temperature differences and increases in maximum velocities.
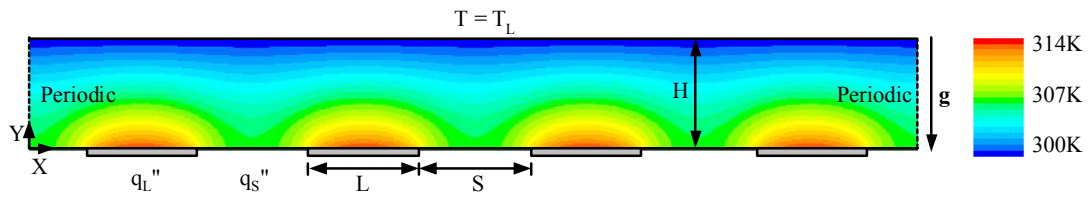
Figure 3.1. A schematic of computational domain showing geometric and thermal boundary conditions with temperature contours plotted for a conduction-dominated regime ($Ra = 0.2$).
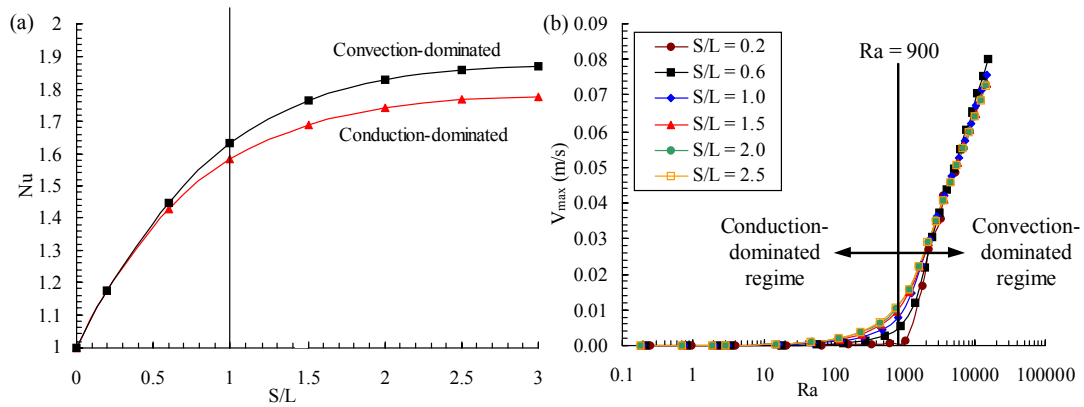
Figure 3.2. The effect on heat transfer and maximum velocity when the spacing between sources is varied while keeping the source length and plenum height equivalent ($L = H$): (a) Heat transfer rates plateau for ratios of spacing to source length greater than one ($S/L = 1$), and (b) Maximum velocity versus Rayleigh number for different source spacings showing the transition from the conduction-dominated regime to the convection-dominated regime occurring at $Ra = 900$.
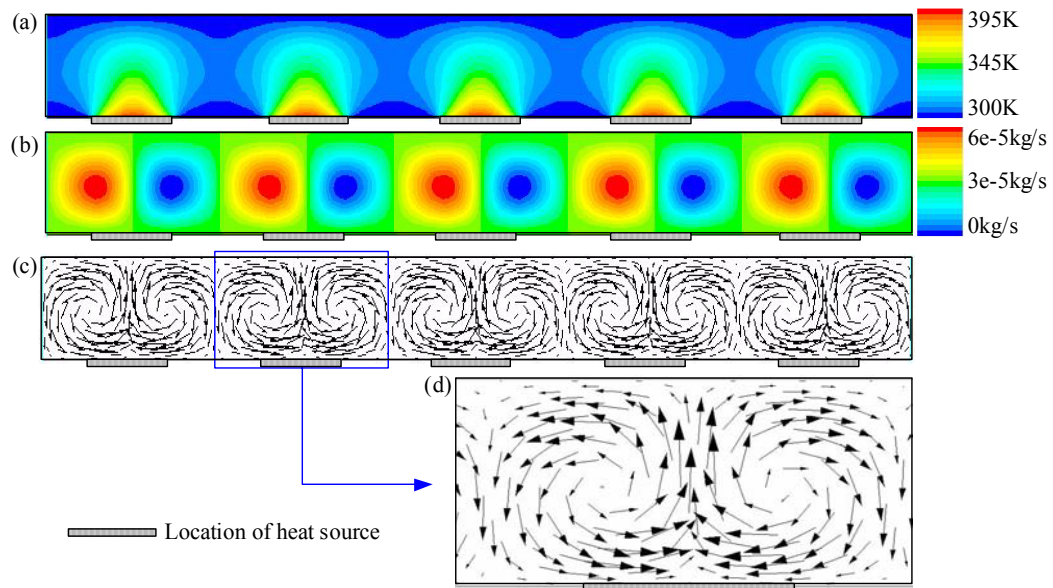
Figure 3.3. Distributed heat sources with uniform heat flux boundary conditions where $S = L = H$ and $Ra = 1350$: (a) Temperature contours, (b) Velocity streamfunctions, (c) Velocity vectors and (d) Velocity vectors surrounding each heat source.
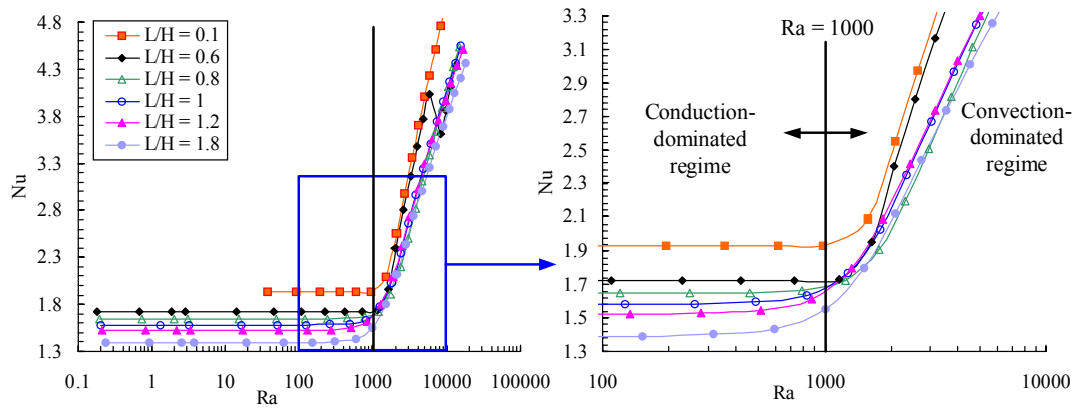
Figure 3.4. Average Nusselt number versus Rayleigh number for various source lengths, L, while keeping the source spacing and source length equivalent ($S = L$). The transition from the conduction-dominated regime to the convection-dominated regime occurs approximately at $Ra = 1000$.
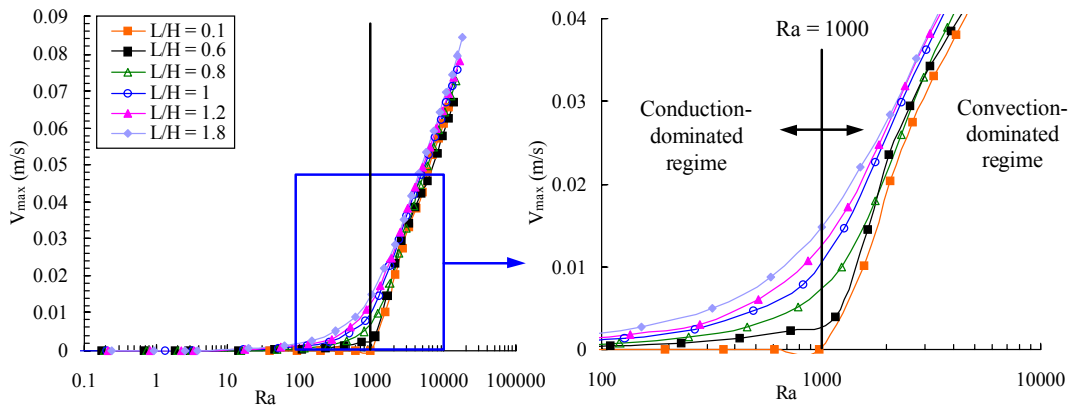
Figure 3.5. Maximum velocity versus Rayleigh number for various source lengths, *L*, while keeping the source spacing and source length equivalent (*S* = *L*). The transition from the conduction-dominated regime to the convection-dominated regime approximately occurs at *Ra* = 1000.
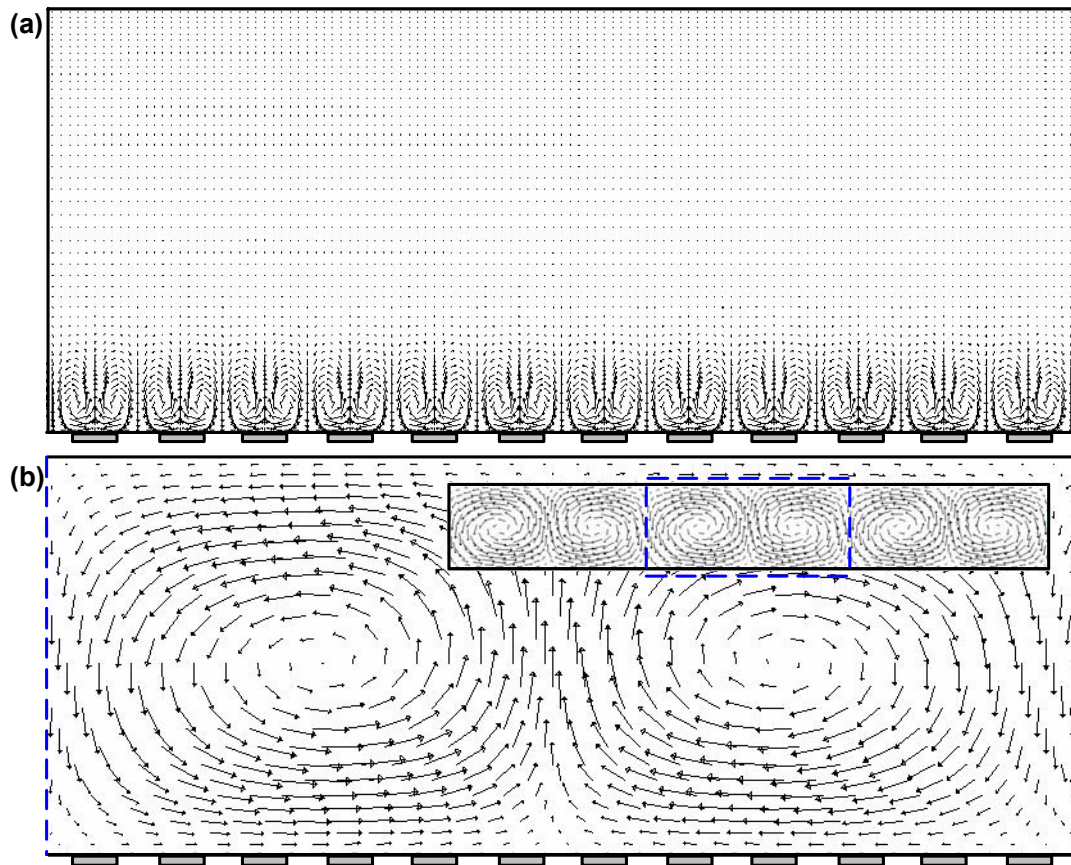
Figure 3.6. Velocity vectors for the $L = 0.1H$ configuration showing the change in Rayleigh-Bénard cell structure and domain size requirements at the transition region: (a) Convection cell pairs develop over each heat source at $Ra = 980$, and (b) Larger Rayleigh-Bénard cells develop over several heat sources at $Ra = 1560$, where a sufficiently large domain is required to avoid artificially small cells. Left and right edges are dashed to indicate that these results are part of a larger domain, shown in the inset figure.
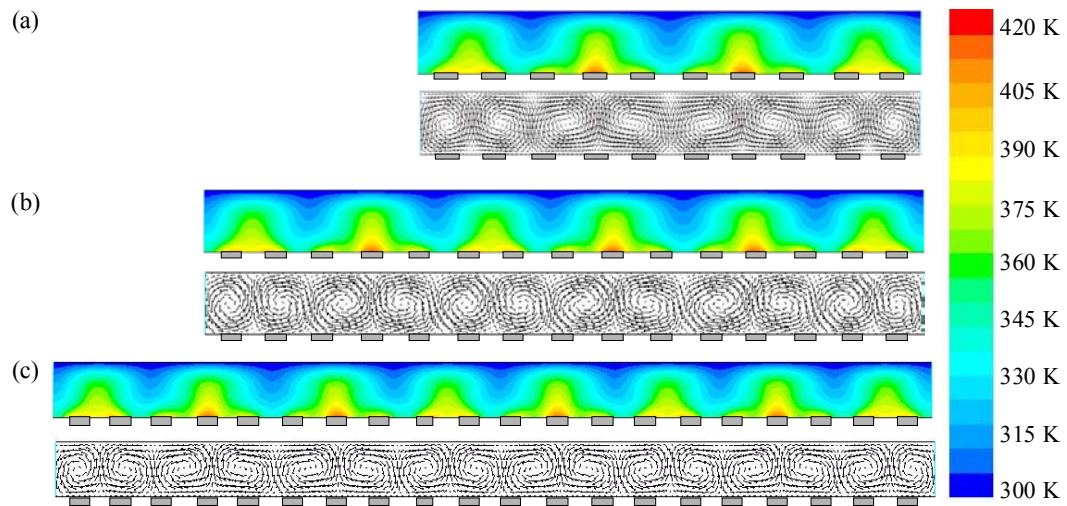
Figure 3.7. Temperature contours and velocity vectors for the $L = 0.4H$ configuration showing bifurcation of Rayleigh-Bénard cell patterns: (a) Domain with 10 heat sources, (b) Domain with 15 heat sources, and (c) Domain with 20 heat sources. It is important to note that the computational domain size is not producing numerical artifacts, rather the computational domain size is influencing the solution in a similar manner as slight differences in geometric tolerances or material properties would bias the flow pattern in a physical cell under these conditions.
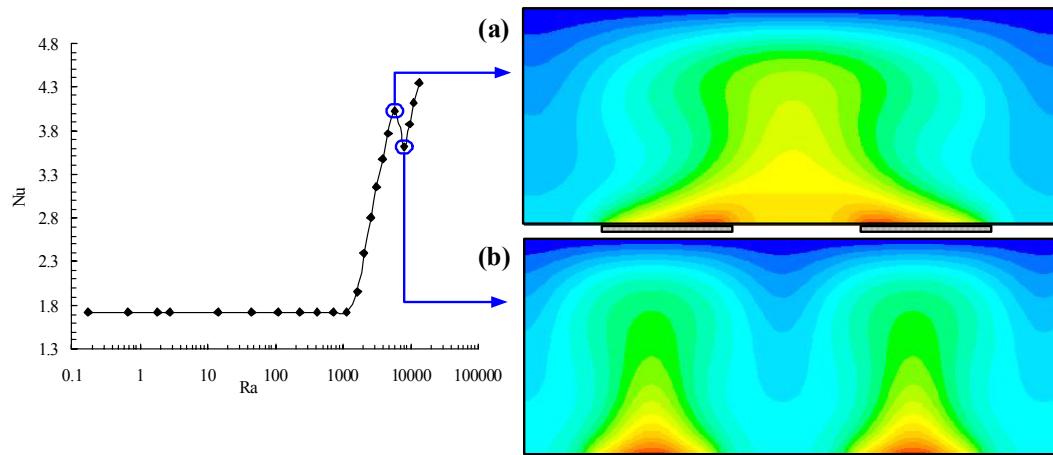
Figure 3.8. Average Nusselt number versus Rayleigh number for $L = 0.6H$ configuration showing the bifurcation of cell structure in the convection-dominated regime and the abrupt change in Nusselt number from 4.0 to 3.6: (a) At $Ra = 5800$, a thermal plume develops over pairs of heat sources, and (b) At $Ra = 8100$, a thermal plume develops over each heat source. This bifurcation is accompanied by an abrupt decline in heat transfer as shown in the plot of Average Nusselt number versus Rayleigh number.
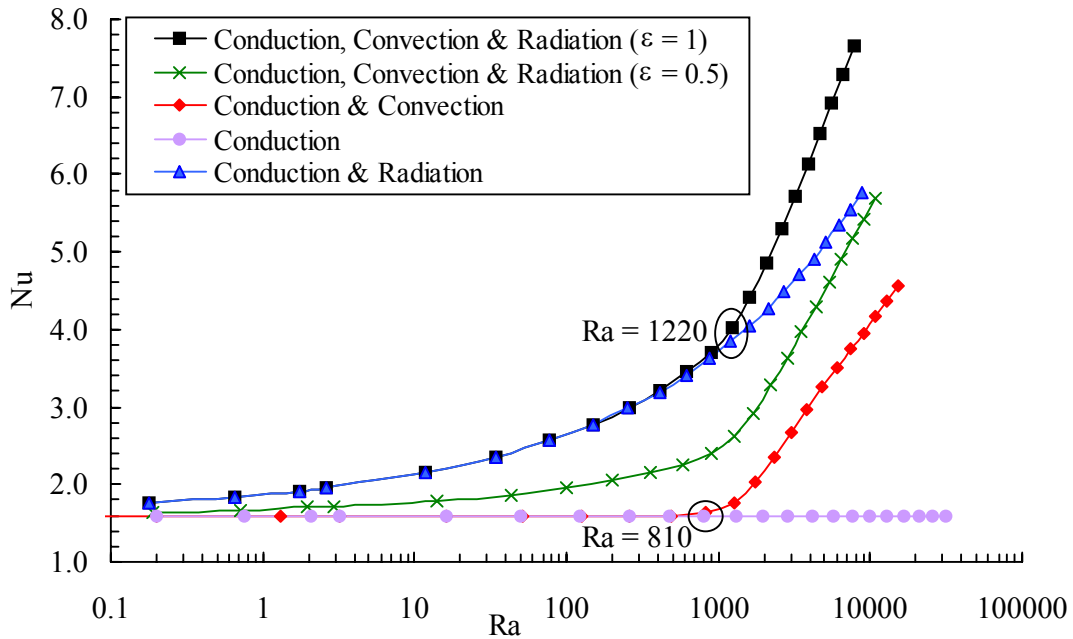
Figure 3.9. Average Nusselt number versus Rayleigh number, while keeping the plenum height, source length and source spacing equivalent ($H = L = S$). The transition from the conduction-dominated regime to the convection-dominated regime occurs approximately at $Ra = 810$ when conduction and convection are simulated, and at $Ra = 1220$ when conduction, convection and radiation are simulated. The critical Rayleigh numbers occurs for a characteristic length of $H = 4$ mm when thermal radiation is not considered, and when all three modes of heat transfer are considered, the critical Rayleigh number occurs for a characteristic length of 5.5 mm. Blackbody radiation on gray surfaces is assumed ($\varepsilon = \alpha_{abs} = 1$).
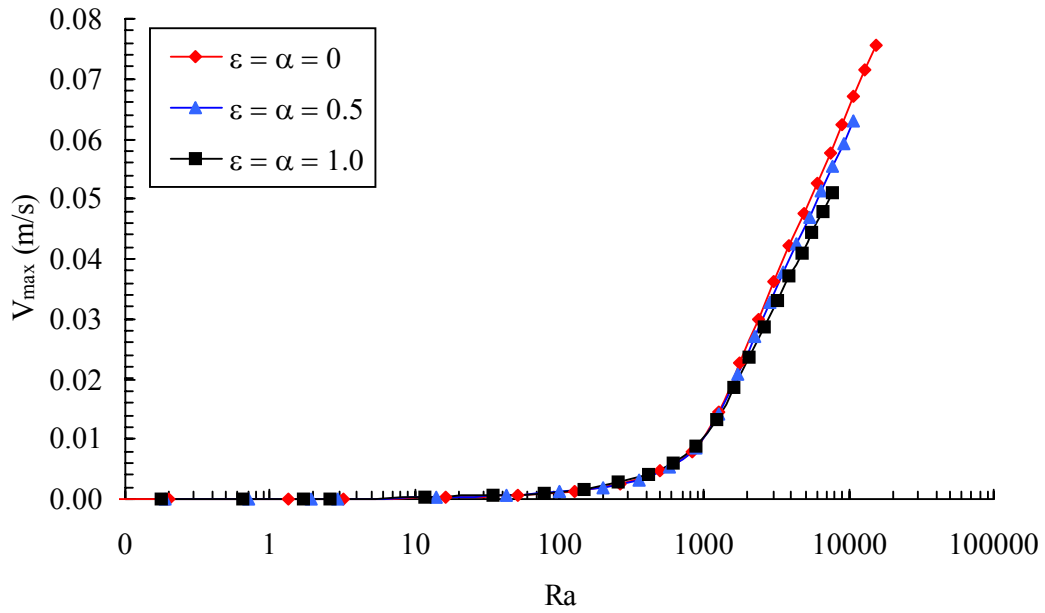
Figure 3.10. Maximum velocity versus Rayleigh number for the configuration where $L = H = S$, showing that as emissivity and absorptivity increase the maximum velocity decreases in the convection-dominated regime.
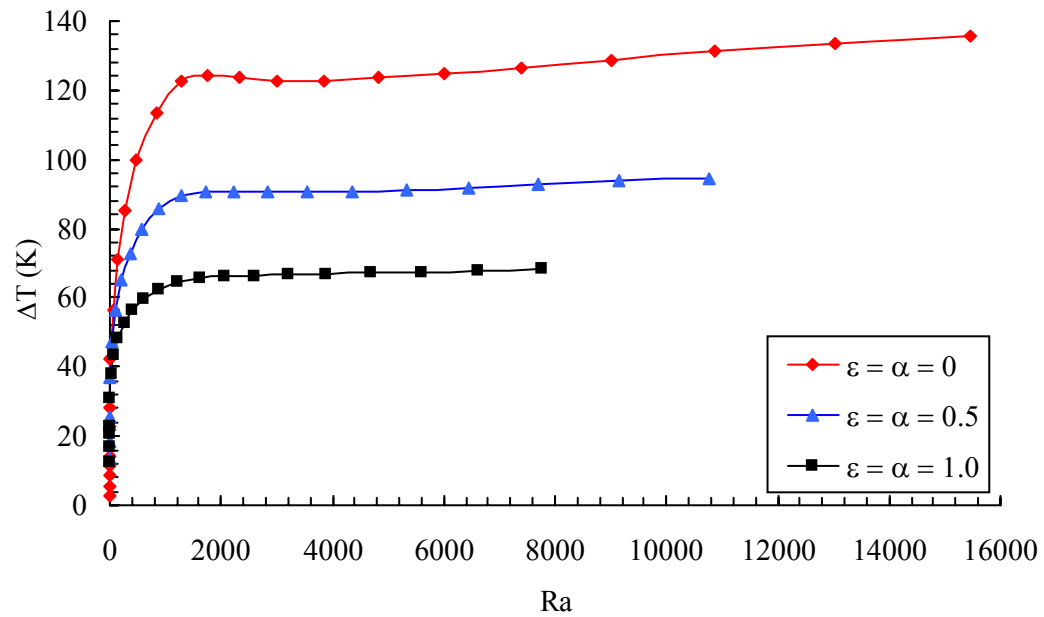
Figure 3.11. Temperature difference versus Rayleigh number for the configuration where $L = H = S$, showing that the maximum temperature difference significantly decreases as emissivity increases.
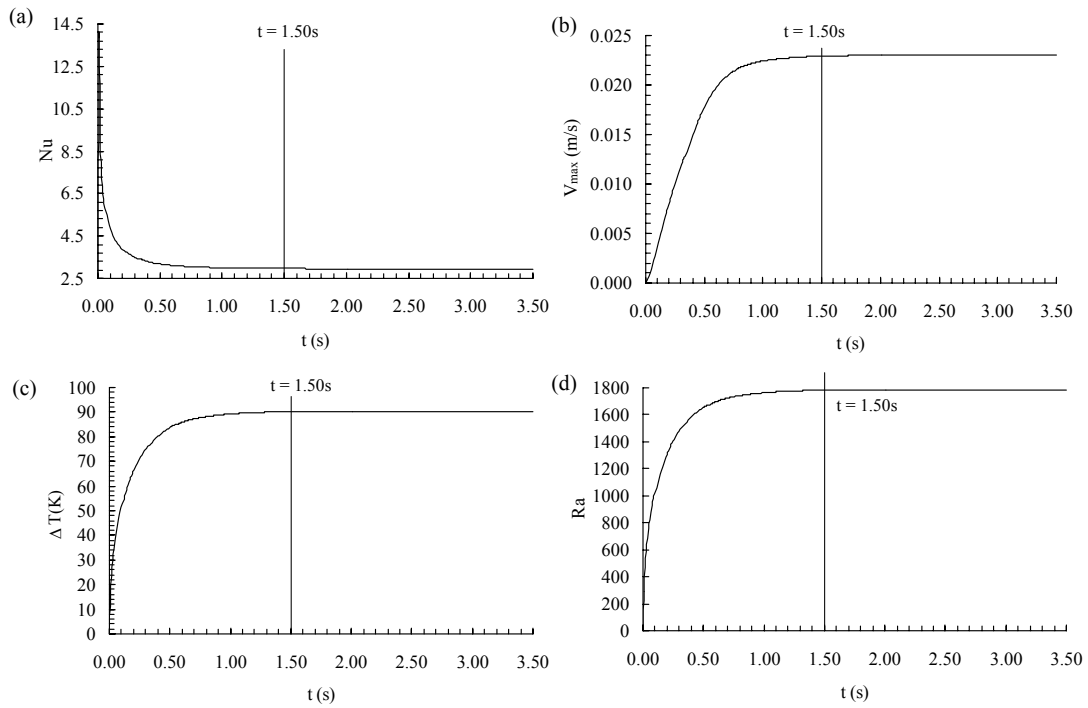
Figure 3.12. Transient response of the two-dimensional model showing that $t = 1.5$ s is required to reach steady state: (a) Nusselt number versus time, (b) Maximum velocity versus time, (c) Maximum temperature difference versus time, and (d) Rayleigh number versus time.
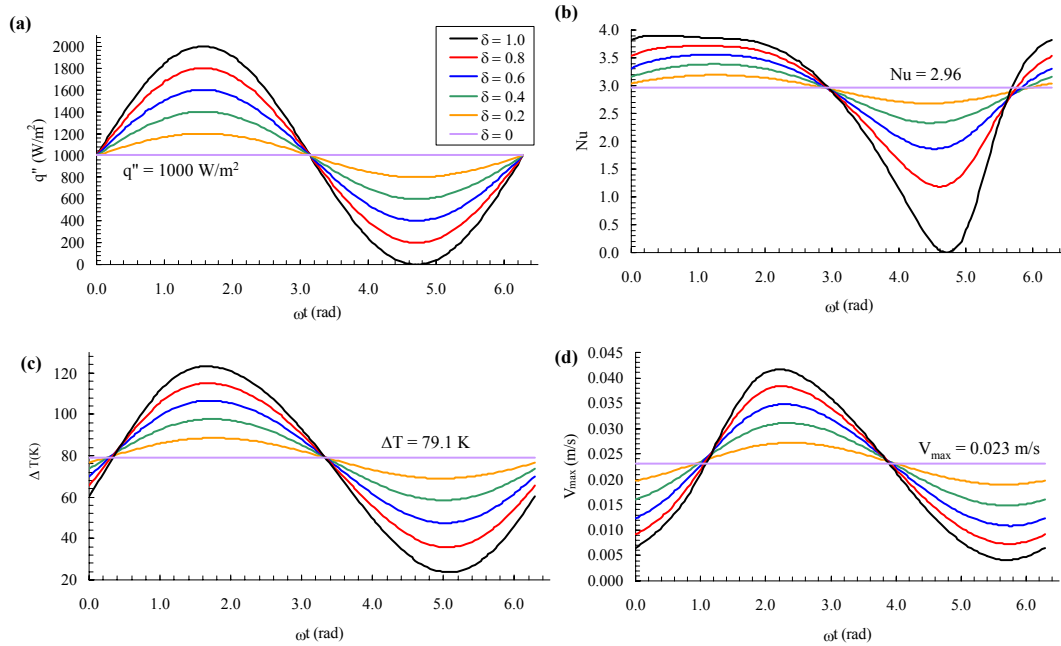
Figure 3.13. Heat transfer effects from varying fuel cell heat flux oscillation amplitude about the steady state value, $\delta = 0$. Results are shown for varying oscillation amplitudes over one full period: (a) Heat flux boundary condition on each fuel cell, (b) Nusselt number, (c) Temperature difference between cold upper wall and area weighted average source temperature, and (d) Maximum velocity.
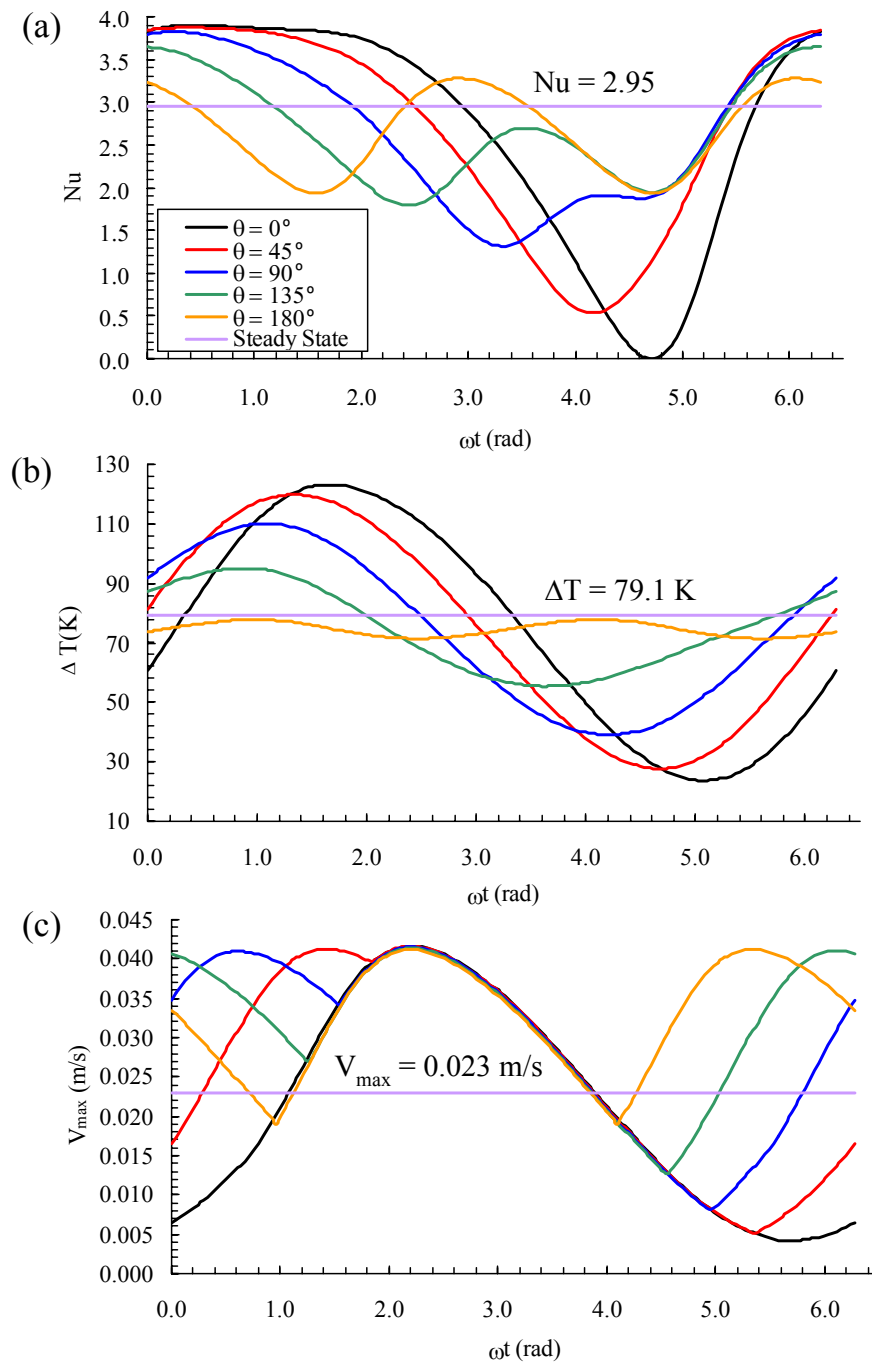
Figure 3.14. Source heat flux sinusoidal modulation effects on heat and mass transfer for alternating sources shifted by 0º, 45º, 90º, 135º and 180º for one period: (a) Average Nusselt number, (b) Temperature difference between cold upper wall and area weighted average source temperature, and (c) Maximum velocity magnitude.

Oscillation Amplitude, δ	Nu_{avg}	% Decrease Nu_{avg}	ΔT (K)	% Decrease ΔT (K)	$V_{max,avg}$ (m/s)	% Decrease $V_{max,avg}$ (m/s)	Ra	% Decrease Ra
0.0	2.957		79.07		0.02302		1562	
0.2	2.952	0.1777	78.83	0.3013	0.02300	0.062	1558	0.3013
0.4	2.932	0.8840	78.34	0.9893	0.02269	1.489	1548	0.9893
0.6	2.893	2.2113	77.45	2.1516	0.02224	3.500	377	2.1516
0.8	2.823	4.5607	76.18	3.8064	0.02175	5.597	1505	3.8064
1.0	2.685	9.2323	74.52	5.9478	0.02136	7.322	1472	5.9478

Table 3.1. The heat transfer effects from varying the oscillation amplitude of heat sources modulated sinusoidally. Compared to the steady state case where $\delta = 0.0$, the Nusselt number, maximum velocity and Rayleigh number decrease with increasing value of oscillation amplitude. On the other hand, the temperature difference between the cold upper wall and the average source temperature decreases. This decrease in temperature difference shows an improvement in heat transfer from the heat sources.

Leading Phase Shift	Nu_{avg}	% Decrease Nu_{avg}	ΔT (K)	% Decrease ΔT (K)	$V_{max,avg}$	% Increase $V_{max,avg}$ (m/s)	Ra	% Decrease Ra
Steady State	2.957		79.07		0.02302		1562	
0	2.684	9.232	74.36	5.948	0.02133	-7.32	1469	5.948
45	2.681	9.355	74.50	5.770	0.02583	12.20	1472	5.770
90	2.671	9.662	74.59	5.656	0.02950	28.14	1474	5.656
135	2.664	9.927	74.61	5.634	0.03182	38.23	1474	5.634
180	2.659	10.078	74.55	5.716	0.03257	41.49	1473	5.716

Table 3.2. The heat transfer effects from varying the phase shift of adjacent heat sources modulated sinusoidally. Compared to the steady state case, the Nusselt number decreases by approximately 10 % when a modulation is introduced. The temperature difference between the cold upper wall and the average source temperature decreases by almost 6 % with modulated heat sources. The maximum velocity increases by about 41 % when the heat sources are out of phase by 180º.

Chapter 4   Conclusions & Recommendations

4.1   Conclusions and Contributions

In Chapter 1, the background and motivation for this thesis were presented, as well as the specific objectives. An overview of the PEMFC was provided, and the trend of fuel cells towards miniaturization was also discussed.

In Chapter 2, one of the first CFD analyses for the membraneless microfluidic fuel cell was presented. Recent experimental studies have established proof-of-concept results; however, poor fuel utilization greatly limits the performance of current designs. Improving fuel utilization while minimizing fuel-oxidant mixing in the microfluidic fuel cell was the focus of this study. A concise electrochemical model of the key reactions and appropriate boundary conditions for the microfluidic fuel cell were developed and implemented into the numerical model. A numerical investigation of the coupled flow, species transport and chemical aspects provided insight into the running parameters and cell geometry required to achieve significantly improved performance.

It was found that the geometry of the cell plays a critically important role in the performance of the cell, which was limited by the mass transport of reactants through the concentration boundary layers to the electrodes. Three geometries were investigated. The straight and rectangular channel geometries simulated in this study are in keeping with current designs. The rectangular geometry with a high aspect ratio in the cross-stream direction is the most promising design for the microfluidic fuel cell, as the reactants demonstrate the least percentage of mixing and the best fuel utilization at the outlet of the fuel cell. With the same hydraulic diameter as the

square geometry, the overall fuel utilization increases by more than a factor of two over the square geometry.

Lowering the inlet velocity results in a significant improvement in fuel utilization with a minimal increase in cross-stream mixing at the outlet. Decreasing the inlet velocity from 0.1 m s^{-1} to 0.02 m s^{-1} causes the fuel utilization to increase non-linearly from 8 % to 23 %, and only causes an increase of 3 % in cross-stream mixing at the outlet. Power output requirements and the diffusive mixing of fuel and oxidant, however, ultimately limit the degree to which the velocity can be reduced. Based on our analysis, a tapered electrode design was proposed. Numerical simulations indicate that significant improvements result from the tapering of the electrodes towards the outlet of the microfluidic fuel cell, while maintaining constant channel cross-sectional dimensions. By tailoring the electrode shape to the reactant concentration profile for an extended cell geometry, the fuel utilization increased from 23 % to 52 %, producing an average current density of 1.1 mA cm^{-2}.

In Chapter 3, a numerical analysis of microconvection patterns associated with distributed fuel cells modelled as flush mounted heat sources in an enclosure was presented. The use of periodic boundary conditions and the investigation of the effect of various geometric parameters and flow parameters has provided new insight on the parameters governing the onset of natural convective flow and associated heat transfer for arrangements relevant to passive cooling for microelectronics. The following conclusions can be drawn from the results obtained from this investigation.

First, it was determined that the source spacing of $S = L$ provides effective convective heat transfer, and was used for the parametric simulations. The heat

transfer rates increase as the spacing length between sources increases, but reach a ceiling for spacing lengths longer than $S = L$. Increasing the spacing beyond this length is of little interest for small scale device design, as it would lead to redundant substrate cost, added weight and volume.

Secondly, the transition from the conduction-dominated regime to the convection-dominated regime occurs within a range of values, which is in contrast to the well-known case of a uniformly heated bottom surface with sidewall confinement. The transition region is recognized as the elbow region of the average Nusselt number versus Rayleigh number. For source lengths of $L = 0.1H$ to $L = 1.8H$, the transition region occurs between Rayleigh numbers 500 to 2000. The range of Rayleigh numbers at which transition takes place decreases as the source length increases. A corresponding transition region occurs in the plot of maximum velocity versus Rayleigh number.

As the source length decreases, the transition region becomes sharper, approaching the familiar bottom wall heating solution [Papanicolaou and Gopalakrishna, (1995)]. The transition elbow region becomes smoother and occurs at lower Rayleigh numbers as the source length increases. In the conduction-dominated regime, the average Nusselt number decreases as the source length increases. The maximum velocity increases at a faster rate as Rayleigh number increases for longer source lengths in the convection-dominated regime.

For short source lengths, the Rayleigh-Bénard cell structure changes at the transition region. In the convection-dominated regime, stronger cell pairs develop over a number of heat sources, replacing the weak and more numerous cells that

appear in the conduction-dominated regime. The dramatic change in Rayleigh-Bénard cell size accounts for the sharp transition and high heat transfer rates in the convection-dominated regime, when compared to configurations of longer heat source lengths. When modelling these flows, care must be taken with respect to choosing the size of the computational domain. The requirements can change dramatically post-transition, and a sufficiently large domain must be chosen to ensure a domain-independent solution.

Bifurcations in cell structure were observed for the configuration of $L = 0.4H$ for Rayleigh numbers beyond 2900; however these solutions did not result in significant changes in the heat transfer rates. At a configuration of $L = 0.6H$, a bifurcation associated with a regime change was observed between Rayleigh numbers 5800 and 8100. The Rayleigh-Bénard cell structure changed from cell pairs developing over heat source pairs at $Ra = 5800$ to cell pairs developing over each individual heat source at $Ra = 8100$. This bifurcation was accompanied by an abrupt decrease in heat transfer, in line with recent work by D'Orazio et al. (2004). The insight this work has provided on the bifurcations associated with this particular geometry are significant design considerations, since in some cases increasing the Rayleigh number instigates a regime transition that results in a decrease of Nusselt number. The multi-physical solutions are due to the non-linearity of the Rayleigh-Bénard problem and their high sensitivity to perturbations, both physical and numerical [Nikfetrat et al., (1995)].

Thermal radiation was added to the mathematical model for the array of distributed fuel cells in the horizontal enclosure studied. Including thermal radiation

in the heat transfer model resulted in an increase in average Nusselt number in both the conduction-dominated regime and the convection-dominated regime. The magnitude of this increase in Nusselt number was more pronounced at higher Rayleigh numbers. The onset of thermal instability in the system was also delayed by including thermal radiation, as the transition from a conduction-dominated regime to a convection-dominated regime occurred at a larger Rayleigh number when compared to the case without thermal radiation.

The effects of heat flux modulation on heat transfer rates were also studied. It was found that Nusselt number, maximum velocity and Rayleigh number decrease with increasing value of oscillation amplitude, while the temperature difference between the cold upper wall and the average source temperature decreases. This decrease in temperature difference shows an improvement in heat transfer from the heat sources.

When a phase shift is introduced between alternating heat sources, the Nusselt number decreases by approximately 10 %. The temperature difference between the cold upper wall and the average source temperature decreases by almost 6 % with phase shifted heat sources. The maximum velocity increases by about 41 % when the heat sources are out of phase by 180º. It is important to note that a decrease in temperature difference is observed, and an increase in maximum velocity is observed, both of which are desirable for heat removal and enhanced reactant transport in the fuel cell design.

4.2   Recommendations

As a result of the work in this thesis, there are many opportunities for future work. Some of these opportunities are outlined below.

The membraneless microfluidic fuel cell is a promising microscale fuel cell design, and with the channel geometry and electrode placement design proposed in this work, experiments can be used to validate these results and to further investigate new designs. Formic acid and oxygen were the fuels modelled in this work, but future work could include an investigation of several other liquid fuels. Further, more in-depth simulations are required to provide additional analysis on current, potential and power densities of the microfluidic fuel cell. Using a recently reported microfabrication process using laminar flow [Kenis et al., (1999)], tailored electrodes may be fabricated with a self-optimizing electrode patterning technique. During the microfluidic fuel cell fabrication process, reactant species are introduced into the left and right inlets with a buffer solution introduced between them. Reactions occurring at the liquid-surface interface produce the desired patterning.

Fuel cells can be integrated into large arrays similar to integrated circuit boards in electronics, and these fuel cell systems can be designed to induce dynamic heat fluxes that can be used to enhance heat and reactant transfer. In this work, horizontal air layers were investigated, but future work can include investigations on the angle of inclination of these air layers as well as the effect of a bulk flow over the fuel cells. Future work can also include designing a system that takes advantage of Rayleigh-Bénard natural convection while being independent of the system's orientation, which is a key consideration in the context of portable power supplies.

This work also included a preliminary study of how heat flux modulation can affect the heat transfer rates in these horizontal air layers. Future work could focus on the heat flux modulation in a wider range of geometries and angles of inclination. Three-dimensional simulations could be used to determine the effects of thermal instability, since the results obtained from two-dimensional simulations are inherently more stable than three-dimensional simulations. The Boussinesq approximation was used throughout these studies. However, since there are potentially large temperature differences within the domain, there is an error associated with using this approximation. For temperature differences greater than 50 K, using the ideal gas law for density and kinetic theory for viscosity and thermal conductivity would result in a much better model. Some preliminary simulations were done using the ideal gas law and kinetic theory; however these simulations resulted in an increase of computational time from 6 h to 85 h. Although using the Boussinesq approximation can lead to an error of approximately 20% in the convection-dominated regime, for the purposes of this study, it was too computationally expensive to use temperature dependent properties. Future work can include using temperature dependent properties, especially if computational processing power is less of an issue.

Electrochemical reaction boundary conditions could also be included in this model to account for fuel cell reactions, and species transport could also be investigated. These studies would lead to an understanding of potential current and power density outputs of the integrated planar microfuel cells. Furthermore, experimental validation would be the key to providing the proof-of-concept for this design.

Bibliography

Adamczyk, Z., Warszynzki, P., Zembala, M. (1999) "Influence of adsorbed colloid particles on streaming potential." *Bulletin of the Polish Academy of Sciences, Chemistry*, 47(3), 239-258.

Arik, M. (2004) "Thermal modeling and performance of high heat flux SOP packages." *IEEE Transactions on Advanced Packaging*, 27(2), 398-412.

Bae, J.H., Hyun, J.M. (2004) "Time dependent buoyant convection in an enclosure with discrete heat sources." *International Journal of Thermal Sciences*, 43, 3-11.

Bahloul, A., Kalla, L., Bennacer, R., Beji, H., Vasseur, P. (2004) "Natural convection in a vertical porous slot heated from below and with horizontal concentration gradients." *International Journal of Thermal Sciences*, 43, 653-663.

Bazylak, A., Sinton, D., Djilali, N. (2005a) "Improved fuel utilization in microfluidic fuel cells: a computational study." *Journal of Power Sources*, 143, 57-66.

Bazylak, A., Djilali, N., Sinton, D. (2005b, Submitted) "Convection in an enclosure with distributed heat sources." *Numerical Heat Transfer*.

Bazylak, A., Sinton, D., Djilali, N. (2005c) "Enhanced microconvection through distributed heat source modulation." American Society of Mechanical Engineers, International Conference on Microchannels and Minichannels, Toronto ON, 1-7.

Bazylak, A., Sinton, D., Djilali, N. (2004) "Membraneless Liquid-Fuel Microfluidic Fuel Cells: A Computational Study." American Society of Mechanical Engineers, International Mechanical Engineering Congress and RD&D Exposition 2004, Anaheim CA, 1-11.

Bird, R.B., Stewart, W.E., Lightfoot E.N. Transport Phenomena, John Wiley & Sons, New York, 1960, 81, 83.

Capon, A., Parsons, R. (1973) "The oxidation of formic acid at noble metal electrodes, part III. Intermediates and mechanism on platinum electrodes." *Electroanalytical Chemistry and Interfacial Electrochemistry*, 43, 205-231.

Casado-Rivera, E., Volpe, D.J., Alden, L., Lind, C., Downie, C., Vazquez-Alvarez, T., Angelo, A.C.D., DiSalvo, F.J., Abruna, H.D. (2004) "Electrocatalytic activity of ordered intermetallic phases for fuel cell applications." *Journal of American Chemical Society*, 126, 4043-4049.

Catton, I. (1972) "The effect of insulating vertical walls on the onset of motion in a fluid heated from below." *International Journal of Heat and Mass Transfer*, 15, 665-672.

Choban, E.R., Markoski, L.J., Stoltzfus, J., Moore, J.S., Kenis, P.A. (2002) *Power Sources Proceedings 2002*, 40, 317-320.

Choban, E.R., Markoski, L.J., Wieckowski, A., Kenis, P.J.A. (2004) "Microfluidic fuel cell based on laminar flow." *Journal of Power Sources*, 128, 54-60.

Cohen, J.L., Westly, D.A., Pechenik, A., Abruña, H.D. (2005) "Fabrication and preliminary testing of a planar membranless microchannel fuel cell." *Journal of Power Sources*, 139, 96-105.

da Silva, A.K., Lorente, S., Bejan, A. (2004) "Optimal distribution of discrete heat sources on a wall with natural convection." *International Journal of Heat and Mass Transfer*, 47, 203-214.

da Silva, A.K., Lorenzini, G., Bejan, A. (2005) "Distribution of heat sources in vertical open channels with natural convection." *International Journal of Heat and Mass Transfer,* 48, 1462-1469.

Deng, Q.H., Tang, G.F., Li, Y. (2002) "Interaction between discrete heat sources in horizontal natural convection enclosures." *International Journal of Heat and Mass Transfer*, 45, 5117-5132.

D'Orazio, M.C., Cianfrini, C., Corione, M. (2004) "Rayleigh-Bénard convection in tall rectangular enclosures." *International Journal of Thermal Sciences*, 43, 135-144.

Dyer, C.K. (2002) "Fuel cells for portable applications." *Journal of Power Sources*, 106, 31-34.

Erickson, D., Li, D. (2002) "Influence of surface heterogeneity on electrokinetically driven microfluidic mixing." *Langmuir*, 18, 1883-1892.

Erickson, D., Li, D. (2003) "Three-dimensional structure of electroosmotic flows over heterogeneous surfaces." *Journal of Physical Chemistry B,* 107, 12212-12220.

Espenson, J.H. Chemical kinetics and reaction mechanisms 2nd Edition*,* McGraw-Hill, Inc., New York, 1995, 200.

Ferrigno, R., Stroock, A.D., Clark, T.D., Mayer, M., Whitesides, G.M. (2002) "Membraneless vanadium redox fuel cell using laminar flow." *Journal of the American Chemical Society*, 124, 12930-12931.

Fluent Inc. (2003) "Fluent 6.1.22"

Fonseca, I., Lin-Cai, J., Pletcher, D. (1983) "A potential step study of the influence of metal adatoms and solution pH on the rate of formic acid oxidation at Pt electrodes." *Journal of the Electrochemical Society*, 130(11), 2187-2192.

Glasstone, S. An Introduction to Electrochemistry, 9th Printing. D. Van Nostrand Company, Inc. Princeton, New Jersey, 1942, 57.

Hahn, R., Wagner, S., Schmitz, A., Reichl, H. (2004) "Development of a planar micro fuel cell with thin film and micro patterning technologies." *Journal of Power Sources*, 131, 73-78.

Hamann, C.H., Hamnett, A., Vielstich, W. Electrochemistry. Wiley-vch, Weinheim, Germany, 1998, 19.

Hanreich, G., Nicolics, J., Musiejovsky, L. (2000) "High resolution thermal situation of electronic components." *Microelectronics Reliability*, 40, 2069-2076.

Harned, H.S., Owen, B.B. The Physical Chemistry of Electrolytic Solutions, 3rd Edition. Reinhold Publishing Corporation, New York, 1958, 228-234.

Heindel, T.J., Ramadhyani, S., Incropera, F.P. (1995a) "Conjugate natural convection from an array of discrete heat sources; part 1 – two- and three-dimensional model validation." *International Journal of Heat and Fluid Flow*, 16(6), 501-510.

Heindel, T.J., Incropera, F.P., Ramadhyani, S. (1995b) "Conjugate natural convection from an array of discrete heat sources: part 2 – a numerical parametric study." *International Journal of Heat and Fluid Flow*, 16(6), 511-518.

Heindel, T.J., Incropera, F.P., Ramadhyani, S. (1996) "Enhancement of natural convection heat transfer from an array of discrete heat sources." *International Journal of Heat and Mass Transfer*, 39(3), 479-490.

Incropera, F.P., Kerby, J.S., Moffatt, D.F., Ramadhyani, S. (1986) "Convection heat transfer from discrete heat sources in a rectangular channel." *International Journal of Heat and Mass Transfer*, 29(7), 1051-1058.

Incropera, F.P., De Witt, D.P. Fundamentals Of Heat And Mass Transfer, John Wiley & Sons, New York, 1990, 559, 827, 828.

Ismagilov, R.F., Stroock, A.D., Kenis, P.J.A., Whitesides, G. (2000) "Experimental and theoretical scaling laws for transverse diffusive broadening in two-phase laminar flow in microchannels." *Applied Physics Letters*, 76(17), 2376-2378.

Jiang, J., Kucernak, A. (2002) "Nanostructured platinum as an electrocatalyst for the electro-oxidation of formic acid." *Journal of Electroanalytical Chemistry*, 520, 64-70.

Johnson, T.J., Ross, D., Locascio, L.E. (2002) "Rapid microfluidic mixing." *Analytical Chemistry*, 74(1), 45-51.

Kenis, P.J.A., Ismagilov, R.F., Whitesides, G.M. (1999) "Microfabrication inside capillaries using multiphase laminar flow patterning." *Science*, 285, 83-85.

Keyhani, M., Prasad, V., Cox, R. (1988) "An experimental study of natural convection in a vertical cavity with discrete heat sources." *Journal of Heat Transfer*, 100, 616-624.

Kulkarni, D.P., Das, D.K. (In Press, 2005) "Analytical and numerical studies on microscale heat sinks for electronic applications." *Applied Thermal Engineering*.

Krishnan, M., Agrawal, N., Burns, M.A., Ugaz, V.M. (2004) "Reactions and fluidics in miniaturized natural convection systems." *Analytical Chemistry*, 76(21), 6254-6265.

Larmine, J., Dicks, A., Fuel cell systems explained 2nd Edition, John Wiley & Sons Inc., Chichester, West Sussex, 2003, 49.

Lee, S.J., Chang-Chien, A., Cha, S.W. O'Hayre, R., Park, Y.I., Saito, Y., Prinz, F.B. (2002) "Design and fabrication of a micro fuel cell array with "flip-flop" interconnection." *Journal of Power Sources*, 112, 410-418.

Lide, D.R. (Ed.), CRC Handbook of Chemistry and Physics, 83rd Edition. CRC Press LLC, Boca Raton, 2002, 5-95.

Litster, S., Pharoah, J.G., McLean, G., Djilali, N. (In Press, 2005) "Computational analysis of heat and mass transfer in a micro-structured PEMFC cathode." Submitted.

Mantle, J., Kazmierczak, M., Hiawy, B. (1994) "The effect of temperature modulation on natural convection in a horizontal layer heated from below: high-Rayleigh-number experiments." *Journal of Heat Transfer*, 116, 614-620.

Markovic, N.M., Ross, P.N.Jr. in: A. Wieckowski (Ed.), Interfacial electrochemistry: theory, experiment, and applications, Marcel Dekker, New York, 1999, 821-841.

Martorell, I., Herrero, J., Grau, F.X. (2003) "Natural convection from narrow horizontal plates at moderate Rayleigh numbers." *International Journal of Heat and Mass Transfer*, 46, 2389-2402.

McDonald, J.C., Duffy, D.C., Anderson, J.R., Chiu, D.T., Wu, H.K., Schueller, O.J.A., Whitesides, G.M. (2000) "Fabrication of microfluidic systems in poly(dimethylsiloxane)." *Electrophoresis*, 21(1), 27-40.

McLean, G.F., Djilali, N., Whale, W., Niet, T. (2000) "Application of micro-scale techniques to fuel cell systems design." *10th Canadian Hydrogen Conference*, 349-358.

Metcalfe, H.C., Williams, J.E., Castka, J.F. Modern Chemistry, Holt, Rinehart and Winston, Inc., New York, 1970, 412.

Nguyen, N-T, Wereley, S.T. Fundamentals and Applications of Microfluidics, Artech House Microelectromechanical Systems Library, 2002, 41.

Nikfetrat, K., Djilali, N., Dost, S. (1995) "Accuracy and nonuniqueness aspects of numerical solutions of some natural convection problems." *Applied Mathematical Modelling*, 20, 371-378.

O'Hayre, R., Braithwaite, D., Hermann, W., Lee, S.J., Fabian, T., Cha, S.W., Saito, Y., Prinz, F.B. (2003) "Development of portable fuel cell arrays with printed-circuit technology." *Journal of Power Sources*, 124, 459-472.

Orszag, S.A., Staroselsky, I. (2000) "CFD: Progress and problems." *Computer Physics Communications*, 127, 165-171.

Ortega, A., Lall, B.S. (1996) "Natural convection air cooling of a discrete source on a conducting board in a shallow horizontal enclosure." *Twelfth IEEE SEMI-THERM Symposium*, 201-213.

Papanicolaou, E., Gopalakrishna, S. (1995) "Natural convection in shallow horizontal air layers encountered in electronic cooling." *Journal of Electronic Packaging*, 117, 307-316.

Pletcher, D., Solis, V. (1982) "A further investigation of the catalysis by lead ad-atoms of formic acid oxidation at a platinum anode." *Journal of Electroanalytical Chemistry*, 131, 309-323.

Rice, C., Ha, S., Masel, R.I., Waszczuk, P., Wieckowski, A., Barnard, T. (2002) "Direct formic acid fuel cells." *Journal of Power Systems*, 111, 83-89.

Roppo, M.N., Davis, S.H., Rosenblat, S. (1984) "Bénard convection with time-periodic heating." *Physics of Fluids*, 27(4), 796-803.

Rosentblat, S., Tanaka, G.A. (1971) "Modulation of thermal convection instability." *Physics of Fluids*, 14(7), 1319-1322.

Sartre, V., Lallemand, M. (2001) "Enhancement of thermal contact conductance for electronic systems" *Applied Thermal Engineering*, 21, 221-235.

Serway, R.A., Physics for Scientists and Engineers / With Modern Physics, Saunders College Publishing, Philadelphia, USA, 1983, 749.

Sharp, K.V., Adrian, R.J., Santiago, J.G., Molho, J.I. in: M. Gad-el-Hak (Eds.), The MEMS Handbook, CRC Press, Boca Raton, Florida USA, 2002, 6-1, 6-2, 6-4.

Shu, Y., Li, B.Q., Ramaprian, B.R. (2005) "Convection in modulated thermal gradients and gravity: experimental measurements and numerical simulations." *International Journal of Heat and Mass Transfer*, 48, 145-160.

Silva, R.F., De Francesco, M., Pozio, A. (2004) "Tangential and normal conductivities of Nafion membranes used in polymer electrolyte fuel cells." *Journal of Power Sources,* 132, 18-26.

Sinton, D. (2004) "Microscale flow visualization." *Microfluid Nanofluid*, 1, 2-21.

Soong, C.Y., Tzeng, P.Y., Hsieh, C.D. (2001) "Numerical study of bottom-wall temperature modulation effects on thermal instability and oscillatory cellular convection in a rectangular enclosure." *International Journal of Heat and Mass Transfer*, 44, 3855-3868.

Stone, H.A., Stroock, A.D., Ajdari, A. (2004) "Engineering flows in small devices: microfluidics toward a lab-on-a-chip." *Annual Review of Fluid Mechanics*, 36, 381-411.

Sun, S.G., Yang, Y.Y. (1999) "Studies of kinetics of HCOOH oxidation on Pt(100), Pt(110), Pt(111), Pt(510) and Pt(911) single crystal electrodes." *Journal of Electroanalytical Chemistry,* 467, 121-131.

Tang, J., Bau, H.H. (1998) "Numerical investigation of the stabilization of the no-motion state of a fluid layer heated from below and cooled from above." *Physics of Fluids*, 10(7), 1597-1610.

Tou, S.K.W., Zhang, X.F. (2003) "Three-dimensional numerical simulation of natural convection in an inclined liquid-filled enclosure with an array of discrete heaters." *International Journal of Heat and Mass Transfer*, 46, 127-138.

Tso, C.P., Jin, L.F., Tou, S.K.W., Zhang, X.F. (2004) "Flow pattern in natural convection cooling from an array of discrete heat sources in a rectangular cavity at various orientations." *International Journal of Heat and Mass Transfer*, 47, 4061-4073.

Waszczuk, P., Barnard, T.M., Rice, C., Masel, R.I., Wieckowski, A. (2002) "A nanoparticle catalyst with superior activity for electrooxidation of formic acid." *Electrochemistry Communications*, 4, 599-603.

Weber, M., Wang, J.-T., Wasmus, S., Savinell, R.F. (1996) "Formic acid oxidation in a polymer electrolyte fuel cell." *Journal of Electrochemical Society*, 143(7) L158-L160.

Appendix A: Joule Heating in Membraneless Fuel Cell

The following discussion shows that the joule heating associated with the membraneless microfluidic fuel cell is negligible. Choban et al. (2004) reported a current density of 4.0 mA cm^{-2} at a working potential of 0.55 V, which resulted in a power density of 2.2 mW cm^{-2}. With an electrode surface area of 0.3 cm^2, this yielded a total power output for one fuel cell to be 0.66 mW.

If approximately 50 % of this power is dissipated as heat, 0.33 mW of heat is generated. The mass flow rate of the solution in this fuel cell with dimensions of 1000 μm x 1000 μm is calculated by:

$$\dot{m} = \rho \, A_{area} U \tag{A.1}$$

$$\dot{m} = \left(998 \frac{kg}{m^3}\right)(1000 \mu \, m)^2 \left(0.1 \frac{m}{s}\right) \tag{A.2}$$

$$\dot{m} = 9.98 x 10^{-5} \frac{kg}{s} \tag{A.3}$$

The temperature difference between the inlet and outlet associated with this heat generation is calculated as follows:

$$\dot{q} = \dot{m} c_p \Delta T \tag{A.4}$$

$$\Delta T = \frac{\dot{q}}{\dot{m} c_p} \tag{A.5}$$

$$\Delta T = \frac{3.3x10^{-4} J/s}{\left(9.98x10^{-5}\dfrac{kg}{s}\right)\left(4180\dfrac{J}{kg°C}\right)} \tag{A.6}$$

$$\Delta T = 7.9x10^{-4}°C \tag{A.7}$$

Using the results of Choban et al. (2004), the thermal effects are negligible. The temperature difference between the inlet and outlet is less than 1/1000 of a degree when it is assumed that the fuel cell is working at 50 % efficiency.

Appendix B: Calculating Electrolyte Conductivity

The following calculations will provide an estimate of the electrolyte conductivity, which is significantly larger than the conductivity of Nafion 117, a commonly used membrane in conventional fuel cells. The approach here is to approximate the conductivity of the electrolyte using the theory of Limiting Ionic Conductance (Kohlraush's Law) [Herbert and Owen, (1958)]. The limiting equivalent conductance of an electrolyte is the sum of two independent factors characteristic of the anion and cation. The following relation is known as the Kohlrausch Law [Harned and Owen, (1958)]:

$$\Lambda^o = \lambda_+^o + \lambda_-^o \qquad (B.1)$$

where, λ_+^o is the limiting conductance of the cation, and λ_-^o is the limiting conductance of the anion. The limiting conductance units are in terms of the more commonly used unit, S/m, which is normalized by concentration, giving $m^2\,S\,mol^{-1}$.

The more general formula is given by [Lide, (2002)]:

$$\Lambda^o = v_+ \lambda_+^o + v_- \lambda_-^o \qquad (B.2)$$

where, v_+ is the number of moles of cations and v_- is the number of moles of anions to which one mole of electrolyte gives rise to in the solution.

To calculate the limiting ionic conductances for $HCOOH_{(aq)}$ and $H_2SO_{4(aq)}$, the following limiting conductances were used:

$$\lambda^o_{H^+} = 349.65\text{x}10^{-4} \text{ m}^2\text{S/mol} \text{ [Lide, (2002)]} \tag{B.3}$$

$$\lambda^o_{\frac{1}{2}SO_4^-} = 80.0\text{x}10^{-4} \text{ m}^2\text{S/mol} \text{ [Lide, (2002)]} \tag{B.4}$$

$$\lambda^o_{HCOO^-} = 52\text{x}10^{-4} \text{ m}^2\text{S/mol} \text{ [Glasstone, (1947)]} \tag{B.5}$$

To make an approximation of the electrolyte conductivity at a particular concentration, the limiting ionic conductivities are multiplied by the concentration that would theoretically be used.

In simulations, a 2.0 M concentration of $HCOOH$ was used. Assuming this concentration of $HCOOH$, the concentration of H^+ is 0.019263 M. Also, from Choban's work (2004), a sulfuric acid concentration of 0.5 M H_2SO_4 was used.

Formic Acid:

$$\sigma_{2.0M \; HCOOH} = \lambda^o_{H^+} * [H^+] + \lambda^o_{HCOO^-} * [HCOO^-] \tag{B.6}$$

$$\sigma_{2.0M \; HCOOH} = 349.65\text{x}10^{-4} \frac{\text{m}^2\text{S}}{\text{moles}} * 0.019263 \frac{\text{moles}}{1\text{x}10^{-3} m^3}$$

$$+ 52\text{x}10^{-4} \frac{\text{m}^2\text{S}}{\text{moles}} * 0.019263 \frac{\text{moles}}{1\text{x}10^{-3} m^3} \tag{B.7}$$

$$\sigma_{2.0M \; HCOOH} = 0.774 \; S/m \tag{B.8}$$

Sulfuric Acid:

$$\sigma_{0.5M\,H_2SO_4} = \lambda^{o}_{H^+} * \left[H^+\right] + \lambda^{o}_{HSO_4^-} * \left[HSO_4^-\right] \tag{B.9}$$

$$\sigma_{0.5M\,H_2SO_4} = 349.65\text{x}10^{-4}\,\frac{m^2S}{moles} * 0.5\frac{moles}{1\text{x}10^{-3}\,m^3}$$

$$+\, 80.0\text{x}10^{-4}\,\frac{m^2S}{moles} * 0.5\frac{moles}{1\text{x}10^{-3}\,m^3} \tag{B.10}$$

$$\sigma_{0.5M\,H_2SO_4} = 21.48\ S/m \tag{B.11}$$

To determine an approximate overall electrolyte conductivity, we average these values.

$$\frac{1}{\sigma} = \frac{1}{\sigma_{2.0M\,HCOOH}} + \frac{1}{\sigma_{0.5M\,H_2SO_4}} \tag{B.12}$$

$$\sigma = 0.747\ S/m \tag{B.13}$$

This conductivity is an estimate of the electrolyte when the concentrations are perfect, that is before any reactions have taken place. This conductivity should decrease as the fluid moves downstream, where more and more fuel has been reacted.

According to the computations above, the conductivity of 0.5 M H_2SO_4 is approximately 21 S/m. According to Hamann et al. (1998), the conductivity of 1.0 M H_2SO_4 is 36.6 S/m at 18 ºC and for 3.5 M H_2SO_4 is 73.9 S/m at 18 ºC. These values are within the same order of magnitude as the estimated conductivity. Clearly, the concentration of H_2SO_4 will have a large effect on the electrolyte conductivity. It is assumed that H_2SO_4 has the dominant affect on facilitating proton transport.

For comparison purposes, it is helpful to know the conductivity of a typical Nafion 117 membrane used in polymer electrolyte fuel cells. Silva et al. (2004) recently reported Nafion 112, 115 and 117 conductivities measured directly on hot-pressed carbon paper/membrane/carbon paper samples immersed in dionized water using impedance spectroscopy. Nafion 117 (with nominal thickness 183 μm) had a conductivity of 4.8 ± 0.1 S/m 25 ºC and 7.9 ± 0.3 S/m at 65 ºC, which is much less than the conductivity of a 1.0 M solution of H_2SO_4.